QUANTITATIVE FRACTURE ANALYSIS OF A BIOLOGICAL CERAMIC COMPOSITE

By

THOMAS JERALD HILL

A DISSERTATION PRESENTED TO THE GRADUATE SCHOOL
OF THE UNIVERSITY OF FLORIDA IN PARTIAL FULFILLMENT
OF THE REQUIREMENTS FOR THE DEGREE OF
DOCTOR OF PHILOSOPHY

UNIVERSITY OF FLORIDA

2001

ACKNOWLEDGMENTS

First, I would like to thank my wife, Aidines. She is my reason. Her love, encouragement, and friendship through the tough times have always been strong and for that I can never truly repay. I would also like to thank my mother for her unending support. She taught me the value of perseverance and hard work among other things, and the values she instilled have been instrumental in where I am today.

Secondly, I would like to thank my professors and mentors, especially Dr. Kenneth Anusavice and Dr. Jack Mecholsky, who provided guidance and much-needed advice whenever asked for. I can never repay the countless hours they spent assisting me, teaching me, and helping to make me a better scientist each day.

Next, I would like to thank Jason Griggs and Alvaro Della Bona. I could not ask for better research partners and friends. And I would also like to thank all the others who have crossed my path along this journey and have been more than friends but very much like family: Allyson, Ben, Zhang, Nicola, Kallaya, and Cliff.

TABLE OF CONTENTS

page

ACKNOWLEDGMENTS ii

LIST OF TABLES v

LIST OF FIGURES vi

ABSTRACT x

CHAPTERS

1 PURPOSE 1

1.1 Research Rationale 1
1.2 Material Selection 2
1.3 Research Objectives 2
1.3.1 Specific Aim 1 2
1.3.2 Specific Aim 2 2
1.3.3 Specific Aim 3 3
1.3.4 Specific Aim 4 3

2 BACKGROUND 4

2.1 Biological Ceramics 4
2.1.1 Introduction 4
2.1.2 Mollusc Shells 5
2.1.3 *Strombus gigas* 6
2.2 Fracture of Biological Composites 8
2.2.1 Composite Analysis 8
2.2.2 Strain Rate 13
2.2.3 Water 14
2.3 Fractal Analysis 16
2.3.1 Fractal Dimension 16
2.3.2 Measurement Methods 18
2.3.3 Fractal Analysis of Brittle Composites 20

3 MATERIALS AND METHODS 22

3.1 Specimen Fabrication 22
3.1.1 Forming 22
3.1.2 Water Storage 23
3.1.3 Protein Removal 24
3.2 Material Properties 24
3.2.1 Density 24
3.2.2 Hardness 27
3.2.3 Elastic Modulus and Poisson's Ratio 27
3.2.4 Crystal Phase Identification 28
3.3 Mechanical Property Determination 29
3.3.1 Flexure Strength 29
3.3.2 Work of Fracture 32
3.3.3 Fracture Toughness 33
3.4 Fractal Analysis 35
3.4.1 Modified Slit Island Method 35
3.4.2 Box Counting Technique Using the Atomic Force Microscope 38

4 RESULTS AND DISCUSSION 40

4.1 Physical Properties Analysis 40
4.1.1 Density 40
4.1.2 Hardness 41
4.1.3 Elastic Modulus and Poisson's Ratio 42
4.1.4 Crystal Structure 46
4.2 Mechanical Properties Analysis 50
4.2.1 Strength 50
4.2.2 Fracture Toughness 54
4.2.3 Work of Fracture 56
4.2.4 Fracture 58
4.2.5 Water 64
4.3 Fractal Analysis 75
4.3.1 Modified Slit Island Analysis 75
4.3.2 Box Counting Technique Using the Atomic Force Microscope 78

5 CONCLUSIONS 79

APPENDIX TABULATED DATA 82

LIST OF REFERENCES 96

BIOGRAPHICAL SKETCH 101

LIST OF TABLES

Table — Page

1. Four-point flexural strength data from *Strombus gigas* specimens stored in air 82
2. Four-point flexural strength data from *Strombus gigas* specimens stored in artificial seawater... 83
3. Four-point flexural strength data from *Strombus gigas* specimens heat treated at 200°C for 24 h..... 84
4. Four-point flexural strength data from *Strombus gigas* specimens stored in deionized water..... 85
5. Four-point flexural strength data from *Strombus gigas* specimens stored in pH4 buffer solution..... 86
6. Four-point flexural strength data from *Strombus gigas* specimens stored in pH10 buffer solution..... 87
7. Four-point flexural strength data from *Strombus gigas* specimens stored in natural seawater..... 88
8. Four-point flexural strength data from *Strombus gigas* stressing rate specimens in water..... 89
9. Four-point flexural strength data from *Strombus gigas* stressing rate specimens in air.. 91
10. Fracture toughness data determined using single edge notched beam.... 94

LIST OF FIGURES

Figure — Page

2.1. Three orders of lamella of the hierarchical structure of the cross-lamellar *Strombus gigas* conch shell 7

2.2. Mechanical behavior of non-transformation toughened laminates based on the laminate structure 12

2.3. Stress-strain diagrams for dry *Strombus gigas* conch in compressive loading at quasi static (a) and dynamic (b) stressing rates 15

2.4. Fracture toughness versus square root of fractal dimensional increment for three groups of materials 18

2.5. Relation of fractal dimension and step length as a function of work of fracture (Currey *et al.*) 21

3.1. Specimen cut in direction parallel to the axis of shell 23

3.2. Thermogravimetric/differential thermal analysis (TG/DTA) graphs (a) prior to heat treatment and (b) post heat treatment 25

3.3. Differential scanning calorimetry (DSC) graphs (a) prior to heat treatment and (b) post heat treatment 26

3.4. Four-point loading configuration 31

3.5. SEM micrograph fracture surface showing microstructural layers 31

3.6 Single edge notched beam configuration to determine fracture toughness of *Strombus gigas* for (a) the weaker inner layer and (b) the stronger middle layer 34

3.7. Optical micrograph (400x) showing the coastline of a polished replica 37

3.8. Plot of log total length versus log step length. The slope is the negative value of the fractal dimensional increment 38

3.9 Representative image of the fractal dimension obtained using the atomic force microscope 39

4.1. Density of *Strombus gigas* as a function of environment in monolithic and powder form 41

4.2. Vickers hardness as a function of indentation load for five environment/temperature conditions 42

4.3 Optical micrograph of indentation with respect tp a) shell microstructure (100x) and b) crush zone (400x) around the indentation 43

4.4. Elastic moduli and Poisson's ratio values for full thickness *Strombus gigas* specimen obtained by ultrasonic measurements 44

4.5 Elastic moduli and Poisson's ratio values for single layer *Strombus gigas* specimen obtained by ultrasonic measurements 45

4.6. X-ray diffraction spectra for *Strombus gigas* powder stored in air. Aragonite crystal structure is the only phase present. 47

4.7. X-ray diffraction spectra for *Strombus gigas* powder heat treated at 200°C for 24 h. Aragonite crystal structure is the only phase present 48

4.8. X-ray diffraction spectra for *Strombus gigas* powder heat treated at 300°C for 24 h. Aragonite crystal structure is the only phase present 49

4.9. Mean strength for *Strombus gigas* specimen stored in air, stored in deionized water, and heat treated at 200°C for 24 h calculated using linear beam analysis, linear beam analysis using middle layer thickness, and composite analysis 52

4.10 Mean strength calculated using linear beam analysis, middle layer linear beam analysis, and composite analysis. Specimens were stored in six environments: air (Air), deionized water (DI), natural seawater (SW), pH4 buffer solution (pH4), pH10 buffer solution (pH10), and artificial seawater solution (ASW). 53

4.11. Mean strength calculated by linear beam and middle layer linear beam as a function of increasing stressing rate. 54

4.12 Mean toughness determined using single-edge notched beam for three conditions: stored in air, stored in deionized water, and heat treated at 200°C for 24 h 55

4.13. Work of fracture for specimen stored in air, stored in deionized water, and heat treated at 200°C for 24 h 56

4.14 Work of fracture for specimens stored in six environments: air (Air), deionized water (DI), natural seawater (SW), pH4 buffer solution (pH4), pH10 buffer solution (pH10), and artificial seawater solution (ASW) 57

4.15. Work of fracture as a function of stressing rate for groups stored in air and in deionized water. 58

4.16 SEM micrograph of the fracture surface of a *Strombus gigas* at a magnification of 20x displaying two distinct fracture surfaces 59

4.17 SEM micrograph of the inner layer of a fracture surface of a *Strombus gigas* at a magnification of 50x 59

4.18 SEM micrograph of the tough middle layer of a fracture surface of a *Strombus gigas* at a magnification of 50x 61

4.19 SEM micrograph of a second order lamella of *Strombus gigas* at a magnification of 2500x 61

4.20 Representative stress-strain diagrams for *Strombus gigas* for three conditions 63

4.21. SEM micrograph at a magnification of 20x showing both first order lamella of *Strombus gigas* stored in deionized water prior to fracture. The presence of the proteinaceous matrix is pervasive. 65

4.22 SEM micrograph at a magnification of 50x of a second order lamella of *Strombus gigas* showing the interconnecting protein 66

4.23. SEM micrograph at a magnification of 2000x showing the strong bonding of the protein with the aragonite crystals of *Strombus gigas* 66

4.24. SEM micrograph at a magnification of 20x showing the presence of the protein on the interface between the inner and middle layers of the *Strombus gigas* 67

4.25 SEM micrograph at a magnification of 200x showing the high organization of protein matrix with the aragonite crystals of *Strombus gigas* 68

4.26 SEM micrograph at a magnification of 800x showing the strong bonding of the protein with the aragonite crystals of *Strombus gigas*. 69

4.27. Representative stress-strain plots for groups stored in air:
(a) stressing rate of 0.02 MPa/s 71
(b) stressing rate of 0.5 MPa/s 71
(c) stressing rate of 20 MPa/s 72
(d) stressing rate of 500 MPa/s 72

4.28. Representative stress-strain plots for groups stored in deionized water:
(a) stressing rate of 0.02 MPa/s 73
(b) stressing rate of 0.5 MPa/s 73
(c) stressing rate of 20 MPa/s 74
(d) stressing rate of 500 MPa/s 74

4.29. Fractal dimensional increment as a function of environment as measured by the modified slit island analysis..... 75

4.30 Fractal dimensional increment as a function of stressing rate as measured by the modified slit island analysis..... 76

4.31. Fracture toughness versus square root of the fractal dimensional increment for both the inner and middle layers for three conditions: stored in deionized water, stored in air and heat treated. Open symbols are inner layer and filled symbols are middle layer values. Diamond - heat treated, Cross - air, and Square - water..... 77

4.32 Fractal dimensional increment obtained for inner and middle layers using both a macroscopic technique (modified slit island) and a microscopic technique (atomic force microscopy) 78

Abstract of Dissertation Presented to the Graduate School of the
University of Florida in Partial Fulfillment of the Requirements for the
Degree of Doctor of Philosophy

QUANTITATIVE FRACTURE ANALYSIS OF A
BIOLOGICAL CERAMIC COMPOSITE

By

Thomas Jerald Hill

August, 2001

Chairman: John J. Mecholsky, Jr.
Cochair: Kenneth J. Anusavice
Major Department: Materials Science and Engineering

The purpose of this study was to analyze the improved mechanical properties of the *Strombus* gigas over non-biogenic aragonite ($CaCO_3$) by controlling and analyzing the presence of the proteinaceous matrix and water.

The specific objectives of this study were to 1) estimate the relative increase of mechanical properties from structure and proteinaceous interface of the *Strombus gigas*, 2) determine if ions in aqueous solution of stress redistribution from the presence of water was the primary mechanism in increasing work of fracture, 3) identify if water activates any viscoelastic effects from the proteinaceous matrix, and 4) identify if the fractal dimension can discern if toughening mechanisms are present in the complex composite.

The *Strombus gigas* system was chosen for this study because it has demonstrated a 10000-fold increase in the amount of energy to cause failure over monoliths composed

of the same basic material. It was concluded that the presence of the protein interface causes an order of magnitude increase in work of fracture, while water increases the work of fracture approximately two-fold over just the protein alone. The water appears to redistribute the stress throughout the structure lowering local stress distribution which was demonstrated by the use of stressing rates. Finally, the fractal dimension appears to be able to discern between some toughening mechanisms occurring in this material.

CHAPTER 1
PURPOSE

1.1 Research Rationale

Notable biological ceramics have several advantages over man-made ceramics. One of the most noted advantages is their strength and toughness and work of fracture. Biological processes control these properties through the intricate and judicious control of multiple levels of structure, viscoelastic interfaces, and the plasticizing effect of water.

Although some of the reasons for the improvement of mechanical properties due to these variables are known, there is still much to be understood. Presently our understanding of the influence of these variables on the mechanical properties and the fracture of these materials is limited. To improve present ceramic composites, it is necessary to understand how these mechanisms contribute to the strength and toughness increase compared with the individual components. The fracture behavior of multi-layer composites can be controlled at many hierarchical levels relative to the microstructure. It has also been demonstrated that polymer interfaces improve the toughness of ceramic composites. Finally, water is a key element in the improvement of mechanical properties. Thus, the understanding of the interaction of length scale, the viscoelastic nature of the polymer, and the role of water in the improvement of toughness in biological composites can aid in the development of new polymer-ceramic composites.

1.2 Material Selection

The *Strombus gigas* conch shell was chosen for this study because its structure has been well studied, and it has demonstrated three orders of magnitude increase in toughness, measured by work of fracture, compared with that of its primary ceramic component, calcium carbonate in aragonite form. This biological composite has demonstrated multiple toughening mechanisms such as crack deflection, fiber pullout, microcracking, and stress transfer.

1.3 Research Objectives

The primary objective of this study was to identify the role of water and the proteinaceous matrix on the mechanical properties and fracture path of the *Strombus gigas* conch shell. A secondary objective was to determine if fractal dimensional increment would correlate to the increased toughening caused by the presence of water and proteinaceous matrix.

1.3.1 Specific Aim 1

Specific Aim 1 was to test the hypothesis that the presence of the proteinaceous interface produces an interface with higher surface area producing a higher strength and work of fracture than just the aragonite crystals in the cross-lamellar structure. This goal was accomplished by removing the proteinaceous material by heating and analyzing the effect of the protein on the strength, work of fracture, and fracture toughness of the *Strombus gigas*.

1.3.2 Specific Aim 2

Specific Aim 2 was to test the hypothesis that aqueous solutions with variable pH and ion concentrations will produce the same increase of work of fracture compared with

specimens stored in air at room temperature. The infiltration of water has two possible toughening mechanisms: stress transfer and protein reconformation.

1.3.3 Specific Aim 3

Specific Aim 3 was to test the hypothesis that water activates the viscoelastic effects of the proteinaceous layer of the *Strombus gigas.* This *Strombus gigas* conch shell was tested and analyzed mechanically for toughness, through work of fracture and strength, as a function of increasing stressing rate. The fracture surfaces were analyzed for evidence of the proteinaceous layer and characterized using fractal analysis.

1.3.4 Specific Aim 4

Specific Aim 4 was to analyze the potential of the fractal dimension to discern between different mechanisms occurring in the hierarchical layers of the *Strombus gigas* and at what microstructural level they are predominant. This aim was accomplished by analyzing the fractal dimension at the macroscopic level using the modified slit island analysis, and the microscopic scale (~5 μm) using the box counting technique on the atomic force microscope for specimens stored in air and deionized water.

CHAPTER 2
BACKGROUND

2.1 Biological Ceramics

2.1.1 Introduction

Fracture of many biological composites containing a high percentage of ceramic material has been studied to determine mechanisms that improve properties, such as fracture toughness, compared with monolithic ceramics of the same composition. If toughening mechanisms from these materials could be incorporated into presently used engineering materials, tougher high-content ceramic composites could be created. Many of the studies on biological ceramic composites have focused on bone, tooth enamel, and many types of shells, such as conch. Both the materials and the structures of these composites have been analyzed using a number of techniques and theories. Though these models have explained some mechanisms associated with these composites, none have adequately explained the thousand-fold increase in work of fracture reported for some of these biological composites compared with monoliths of the same material. Sarikaya and Aksay[1] stated that:

> "A quantitative understanding of the toughening and strengthening mechanisms in nacre is necessary because these mechanisms depend upon the structural relationships of the organic and inorganic phases. Mechanical property evaluation of the overall shell, particularly under dynamic conditions in which the organism lives and makes use of its multifunctional characteristics, is also essential for the design of multifunctional materials through biomimicing. Future research should include proper testing techniques for measuring interfacial properties, analysis of paths for crack propagation, and their micromechanical analysis." (pp. 73-74)

In Chapter 4 of Biomimetics: Design and Processing of Materials,[1] over 135 articles were referenced relative to the properties, crystallography, morphology, and formation of nacre demonstrating that much research has been performed in this area. One conclusion that is drawn by the authors of this chapter is that more research is needed to characterize the mechanical properties, especially with respect to a quantitative understanding of toughening and strengthening of the structure. Sarikaya, Liu, and Aksay concluded that future research should include analysis of interfacial properties, crack propagation, and micromechanical effects.

2.1.2 Mollusc Shells

Bøggild (1930)[2] was the first to analyze the structure of many different mollusk shells. Since that initial study, biologists have performed many studies on the various properties of shells, but it was not until in the mid-1970s that Currey[3] began to correlate the mechanical properties of mollusc shells with the microstructure of the shells. Since then, many studies have been performed on various biological ceramic composites, such as teeth, bones, and shells, which have attempted to model the structures and predict the mechanisms that produce increased mechanical properties.

There are five major types of structures in mollusk shells: prismatic, nacreous, cross-lamellar, foliated, and homogenous. Of these types, two have been studied for comparison with mechanical properties – the nacreous and the cross-lamellar. This is because of their vast increase in strength and work of fracture. The nacre structure has demonstrated a 3000-fold increase in work of fracture of aragonite, with flexure strength values in the range of 200-250 MPa. The cross-lamellar structure has demonstrated a 10000-fold increase in work of fracture over the aragonite crystal, but strength values in

the range of only 100-120 MPa [4]. Though the nacre structure has been extensively analyzed, the cross-lamellar structure has received limited investigation on the correlation of the microstructure and toughening mechanisms with the properties of this natural mineral.

The first study to analyze the mechanical properties was performed by Currey and Kohn.[5] They correlated the fracture patterns with the crack propagation behavior of the *Conus* shell which exhibits a cross-lamellar structure. They explained that the strength results were a function of the middle layer and that the outer layer adds very little strength to the composite structure. They did not measure the fracture toughness or work of fracture.

Jackson et al.[6] were the first to model the mechanical properties of nacre using shear-lag models developed for composites with plate shaped crystals. They assumed that pullout was the main mode of failure and that the effect of water is to increase the ductility of nacre by the associated introduction of plastic work.

2.1.3 *Strombus gigas*

Though the nacre structure has been continuously studied, it was not until Laraia and Heuer[7] in 1989 that someone resumed the study of the cross-lamellar structure in the *Strombus gigas*, shown in Figure 2.1. They stressed their specimens in four-point bending and determined that the shell exhibited a combination of toughening mechanisms, such as crack bridging, microcracking, fiber pullout, microstructurally induced crack arrest, and branching, to cause the orders of magnitude increase in toughness over single-crystal aragonite, which makes up 99.9 wt % of the structure.

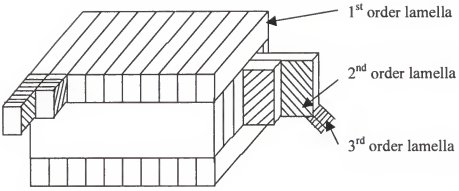

Figure 2.1 The three orders of lamellae of the hierarchical structure of the cross-lamellar *Strombus gigas* conch shell

In 1994, Kessler et al.[8] analyzed the hierarchical structure of the *Strombus gigas* shell. They tested the specimen both dry and wet and defined two failure stages in the shell for each condition. In the dry specimen, multiple crack channeling occurred in the first stage, while in the wet shell, a major crack grew with some microcracking followed by a crack delamination at the interface between the first and middle layers. In the second stage for both wet and dry conditions, the growth of a major crack was surrounded by some minor cracks through the middle layer to produce fracture. They demonstrated that the specimen in the wet condition had a greater deflection and work of fracture.

In 1996, two papers were published simultaneously on a study done by a group studying the *Strombus gigas*. One paper by Kessler et al.[9] modeled multiple crack energy dissipation using the *Strombus gigas* as its biological example. The model was based on the investigation of multiple cracking of thin films performed by Thouless et al.[10] The

second paper by Kuhn-Spearing et al.[11] correlated the large fracture resistance to the extensive microcracking that occurs along the numerous interfaces within the microstructure. They estimated the energy to produce the measured delamination and channel cracks, and then developed a model to determine the influence of these mechanisms on the work of fracture. They concluded that only five percent of the total work of fracture was attributed to the delamination, and that the rest of the high toughness is associated with the remaining middle layer and the non-linear energy mechanisms associated with the fracture surfaces.

Heuer's group[12] used transmission electron microscopy and bending experiments to quantitatively analyze the resistance to catastrophic failure of the *Strombus gigas* by taking into account two energy dissipating mechanisms: microcracking of the inner layer and crack branching of the middle layer.

Menig et al.[13] correlated the mechanical response of the *Strombus gigas* in a dry state with its high damage tolerance and microstructure. They used quasi-static (3-300MPa/s) and dynamic ($10 \times 10^3 - 25 \times 10^3$ GPa/s) stressing rates in compression along with three point bending tests. They determined that the conch exhibited strain rate sensitivity in compression and that crack deflection, delocalization of damage, and viscoplastic deformation of the organic layers were the most important mechanisms.

2.2 Fracture of Biological Composites

2.2.1 Composite Analysis

The lack of toughness has historically been known to be a disadvantage for using ceramics in any load-bearing application.[14-19] Composites are known to produce improved mechanical properties compared with monoliths of the same materials. Ceramic composites have produced marked increases in strength, toughness and work of

fracture. These composites have demonstrated a flaw size independence over a wide range of indentation loads, i.e., R-curve behavior. The R-curve phenomenon would allow many ceramics materials to be used in which the formation of flaws and cracks could be realized before complete failure occurs.

Ceramic composites can be grouped into two broad categories: (1) a major brittle phase with a brittle reinforcement phase; and (2) a major brittle phase with a ductile reinforcement phase. The bonding between these phases is very important to the mechanical properties of the composite. Brittle/brittle composites produce an increase in toughness when a weak interface is present.[14,15,20-24] The weak bonding introduces an interface for the toughening mechanism of delamination and crack deflection. In well-bonded brittle/brittle ceramic composites, a propagating crack will continue through the material without the formation of new surface area during failure thereby producing low toughness. The brittle/ductile composites produce increased toughness in a similar manner as the brittle/brittle composites with an inelastic or viscoelastic component introduced during the fracture process.

Toughening increases from energy dissipation upon the formation of a crack in a composite structure can be analyzed using the stress-displacement constitutive laws. The change in mechanical energy (U_m) relative to change in crack size can be defined as:[20]

$$J = \frac{dUm}{dc} = \int_s \left[U dy - F\left(\frac{du}{dx}\right) \right] \tag{1}$$

where s is the boundary of the material around the crack tip, U is the strain energy per unit volume and $F(u)$ is the traction force vector.

Using equation (1) for the toughening contribution of a composite material that exhibits a bridging mechanism, the increase in mechanical energy dissipation can be determined using a path independent J integral[20]:

$$J = 2\int_0^{u^*} p(u)du \tag{2}$$

where $2u^*$ is the crack at the edge of the bridging zone and $p(u)$ is the resisting stress from the bridging mechanisms that must be overcome to continue crack propagation. Further, the toughening contribution from bridging can be described in the nondimensional form.

$$J = \frac{\chi_w}{\sigma_d A} \tag{3}$$

where σ_d is the yield strength of the ductile phase, A is the cross section of the ductile phase, and χ_w is a work of rupture factor depending on the bonding at the interface and ductility of the reinforcing phase. This work of rupture factor allows the yield strength and bonding of the ductile phase to be integrated into the toughness contribution of the composite.

A summary of the mechanical behavior of the four types of composite failures of non-transforming toughened laminates based on the type of interface and reinforcing phase was developed by Mitchell[25], shown in Figure 2.2. The proposed toughening mechanisms and diagrams of the stress-strain relation are presented for each case.

For the first case, a weak brittle/brittle composite, five toughening mechanisms are present: microcracking, crack arrest, interface delamination, interface friction, and crack reinitiation. These mechanisms occur along the weak interfaces, but these interfaces are also the limiting factors for producing greater fracture resistance. Though

this type of composite produces improved properties over the monolith, it still only gives moderate toughness and the lowest strength in comparison to all the composites.

The second case, a brittle/brittle composite with a strong interface, has even fewer toughening mechanisms: microcracking and crack deflection. These types of composites have the lowest toughness of the composites and only moderate strength. Unless crack deflection occurs with bifurcation, only a single crack will propagate through the material producing a low work of fracture.

The third case is the brittle/ductile composite with a weak interface. This produces the highest values of toughness, strength, and work of fracture. These types of composites have the most potential for improved mechanical properties because of the numerous mechanisms include crack arrest, microcracking, interface delamination, fiber pull out, ductile bridging, yielding, crack tip blunting, and crack reinitiation. The failure of these types of composite can vary greatly. The yield strength of the plastic phase is critical to how the composite fails. As the yield strength of the plastic phase increases, the ductility of the phase decreases, limiting the deformability of the entire composite, but increasing its strength. When the brittle/ductile composite interface is strong the highest strength is produced, but the toughness is reduced with respect to a composite with a weak interface. In the strong interface case, the crack does not propagate along the interface between the materials, but produces a surface with limited bridging and yielding.

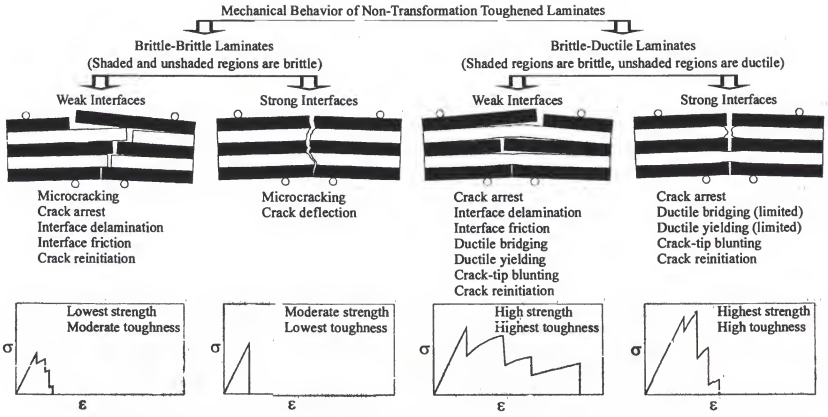

Figure 2.2. Summary of the mechanical behavior of non-transformation toughened laminates based on the structure of the laminate.

2.2.2 Strain Rate

Many biological ceramic composites show viscoelastic behavior that suggests their toughness should be a function of strain rate. The dependence of this function of strain rate will be affected by the amount of plasticizer (water) present. At high strain rates, cracks do not follow any particular path through the composites structure, while at low strain rates the fracture surface is very convoluted and rough, following the interfaces of the structure.

Most studies on the strain rate dependence of biological ceramic composites have been performed on types of bone. Robertson and Smith[26] examined at the effect of strain rate on the stress-strain curves of cow leg bone. They found that at high strain rates the curve was linear with a brittle type of failure. At low strain rates the stress-strain curve was non linear and the bone yielded at higher strains. The transition between these two modes of fracture occurred at a strain rate of about 2.5×10^3 s^{-1}. Behiri and Bonfield[27] reported that the toughness of the cow leg bone increases as the velocity of the crack tip increased up to a value of about 1.2 mm/s^{-1}, where the propagation of the crack becomes unstable and turns from being rough to glassy, and the fracture toughness decreases. Caler and Carter[28] produced a cumulative damage model for the fracture of bone. It predicts that bone will accumulate damage over time when stressed even at low stress and that bone will fracture when a certain amount of damage has occurred. A low strain rate will allow more time for damage to accumulate at any particular stress than at high strain rates. Therefore low strain rates should produce lower strengths.

Menig et al.[13] analyzed the *Strombus gigas* in order to design and synthesize multi-functional composites tailored to optimize structural plus ballistic and/or blast-

resistant applications. They chose stressing rates of 6-400 MPa/s, a "quasi-static" compression, and 15-25 x 10^3 GPa/s, a dynamic impact compression. The specimens, all from one shell, were loaded in two directions, parallel and perpendicular to the surface, in a dry condition. Figure 2.3 shows the stress strain diagrams for the perpendicular direction using the quasi-static and dynamic loading rates. Both groups have maximum stress values at a strain of about 0.01, with the higher stressing rate producing higher strengths.

2.2.3 Water

Water is a constituent in all biological materials. It serves many functions in the growth and maintenance of these materials. Water can have three effects on the mechanical properties of a biological material:

(1) Water can pre-stress a fiber matrix structure. The matrix or proteinaceous phase can bind large amounts of water causing an osmotic swelling against the restraining fibers which are put in tension to give a pre-stressed system. This mechanism occurs in cartilage, where the water content is as high as 65-80%. Strengthening by water uptake is little used in high ceramic biological composites.

(2) The water can flow through narrow channels in the composite, redistributing the stress, thereby delocalizing the stress at any one area. Fox[29] proposed this mechanism for toughening in the structure of enamel, stating that the energy absorbing capacity of enamel depends upon the expulsion of liquid from between the mineral fibers. He also demonstrated that the electrical double layer on the surface of the fibers could greatly influence the toughness by the addition of fluoride ions.

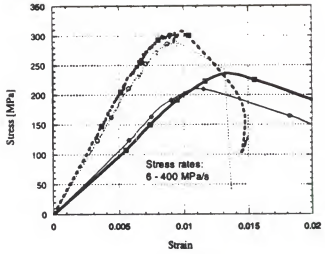

a) stressing rate of 6-400 MPa/s

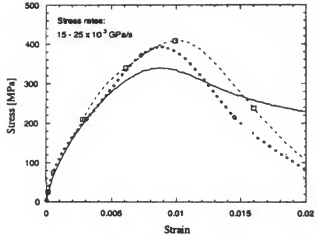

b) stressing rate of 15-25 x 10^3 GPa/s

Figure 2.3 Stress-strain diagrams for dry *Strombus gigas* conch in compressive loading at (a) quasi static and (b) dynamic stressing rates (Menig et al.[13])

(3) The water/protein interactions can greatly affect the mode of fracture in biological composites. This can be due to at least two effects of water bound in the system: the interpolation of water molecules into H-bonded linkages between side groups, such as amide and carbonyl groups, thus effectively breaking H-bonds, and the provision of extra space around the side chains, thus allowing more freedom of rotation about the bonds in the protein backbones and side chains. Both effects cause the water to plasticize the material producing greater ductility.

It is clear from the previous studies that much more research still needs to be performed to correlate these mechanisms with mechanical properties obtained in the presence of water.

2.3 Fractal Analysis

2.3.1 Fractal Dimension

Fractal geometry is non-Euclidean geometry which can quantitatively define irregular shapes and surfaces. Fractal objects are self-similar (or self-affine) and scale invariant, and are characterized by a non-integer dimension. A self-similar surface is one in which the length scaling is isotropic and remains invariant under the transformation (x, y, z) to (ax, ay, az), where a is the scalar constant. A self-affine surface is one in which the length scale is planar and remains invariant in that plane. A scale invariant object is one in which the surface will look statistically the same on any magnification scale.

Fractal dimensions have been used to describe many physical phenomena such as Brownian motion, cloud surfaces, surfaces of porous catalysts, soot particles, colloidal silica aggregates, percolation clusters, lengths of coastlines and fracture surfaces. The

fracture of brittle materials is one area of extensive study. The topography produced during brittle fracture has been studied by many scientists using fractal geometry. The fractal dimensional increment has been correlated to the fracture toughness by Mecholsky[30-32] through the following equation:

$$K_{IC} = Ea_0^{1/2} D^{*1/2} \tag{4}$$

where K_{IC} is the fracture toughness, E is the elastic modulus, D^* is the fractal dimensional increment, and a_0 is a characteristic fracture length. Many brittle materials have been plotted using this equation as shown in Figure 2.4. These materials include glasses, glass-ceramics, polycrystalline ceramics, and single crystal ceramics. The fractal dimension is part of a characterization tool that can describe the path of a propagating crack and is not unique.

Fractal geometry has shown good correlation between the fractal dimension, toughness and microstructure when one characteristic is changed in one baseline material. Thompson et al.[33] stated that the fracture energy varied linearly with fractal dimensional increment in lithia disilicate glass-ceramic systems when different heat treatments were used to obtain different crystal volume fractions. Hill et al.[34] showed in the baria silicate glass-ceramic system that the fractal dimensional increment varied linearly with the aspect ratio of crystals produced by different heat treatments. Mecholsky and Mackin[35] examined the fractal dimension of chert with a decrease in fracture toughness caused by heat treatment. They determined that the fractal dimensional increment decreased with fracture toughness. Chen and Mecholsky[36] studied the mechanical bonding at the interface of nickel-alumina laminates using fractal analysis and then measured strength and work of fracture to determine which interfaces produce the most desired results.

They concluded that the deformation and fracture results of the composites showed conformity to tensile models and revealed that the toughness and strength of the composites were a function of the interfacial tortuosity.

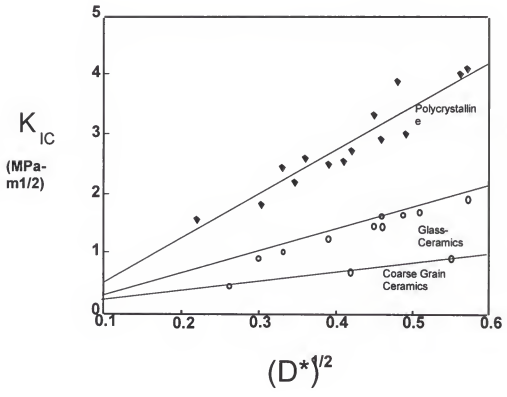

Figure 2.4 Fracture toughness versus square root of fractal dimensional increment for three groups of materials.

2.3.2 Measurement Methods

A variety of techniques to obtain the fracture surface contours have been reported.[37-43] Most boundary contours are obtained using one of two contour planes: parallel to the plane of fracture (slit-island) or perpendicular to the plane of fracture (profile). These boundaries are analyzed using a variety of techniques to determine the

fractal dimension. One of the most popular techniques for quantifying the boundary was introduced by Richardson.[44]

Some studies have used vertical profiles to produce contours that were measured by a form of Richardson analysis. Clarke[37] obtained a series of vertical profiles, which were analyzed using the Richardson technique. He averaged the values and added 1 to obtain a dimension. Denley[39] used line scans obtained by scanning tunneling microscopy (STM). From these vertical scans, he determined a parameter from the relative surface area obtained as a variation of measuring length. Alexander[40] also applied the Richardson method to elevation profiles that resulted in curved lines from which he used the central portion as an estimation of the fractal dimension. Tanaka[41] determined the fractal dimension of soda-lime glass and a tungsten-carbide cobalt metal using a Richardson analysis of a crack trace produced by a diamond pyramid indentation. However, Russ[45] points out that using the vertical profile of the fracture surface will not produce the same results as the horizontal. It has been demonstrated that errors in measurement can be obtained if careful and proper techniques are not followed[46,47]. Care must be taken to measure the appropriate surface.

Other techniques use surface plots instead of line profiles to calculate the fractal dimension. Shapes such as pyramids and boxes of standard sizes are then arranged across the surface to determine the total amount of surface area for each sized shape, which is then plotted similarly to the Richardson equation. The atomic force microscope uses a box counting technique to produce its fractal dimensions.

2.3.3 Fractal Analysis of Brittle Composites

Very few studies have used fractal analysis to study biological ceramic composites, and most of those have been on bones, their microstructure and fracture. Lespessailles et al.[48] used fractal geometry to analyze the microarchitecture of trabecular bone as a determinant of bone fragility, but the only study to attempt to study the fracture of a biological ceramic composite with the fractal dimension was performed by Currey et al.[49] They studied the fracture surfaces of a variety of bone materials and antlers with various mineral contents using fractal geometry. They measured the change in fractal dimension with respect to step length for the bones with a range of work of fractures, as shown in Figure 2.5. They noted that the bony hard tissues with a high work of fracture had a large fractal dimension at the larger step lengths and smaller dimensions at the lower step lengths. Tissues with the lower work of fractures had lower fractal dimensions, which increased as the step length scale decreased. They concluded that the bony hard tissue with the high work of fracture had a low fractal dimension at large step lengths because the components of those tissues peel away from each other rather easily causing the stress concentrations to be blunted at the microscopic level. Therefore, the strain energy stored in the specimen increases much less rapidly than the total work under the stress-strain curve required to drive a fatal crack.

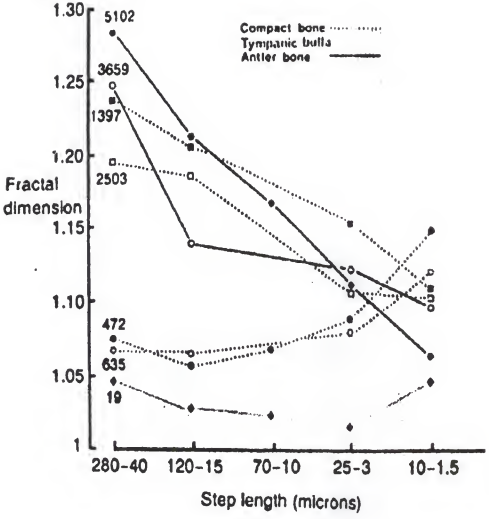

Figure 2.5 Relation of fractal dimension to step length as a function of work of fracture (Currey et al.[49])

CHAPTER 3
MATERIALS AND METHODS

3.1 Specimen Fabrication

3.1.1 Forming

Flexure bars were produced from untreated *Strombus gigas* conch shells. The specimens were cut parallel to the longitudinal direction of the shell axis as shown in Figure 3.1. The outer whirl of the shell was removed first and subsequently sectioned into specimens approximately 50 mm long by 8-9 mm wide with a variable thickness depending upon the shell. The outer lip of the last whirl was not used because the structure of the shell deviates in thickness and in the structure of this portion of the *Strombus gigas,* another layer is present. A Fibre Cut reinforced cutting disc (Dedeco) was used at low speed to produce the specimen. The specimens were continually immersed in water during the process to help minimize the initiation of any cracks from any temperature increase.

After sectioning, the widths of all specimens were polished to 6 mm using 320 grit SiC abrasive. The upper surface of the test bar, i.e., the surface placed in compression, was finished using 320 and 600 grit SiC abrasive to remove surface irregularities and produce specimens between 2 mm and 3 mm thick. The first order lamina on the exterior of the specimen was removed during this step on most of the specimens.

The surface to be placed in tension was polished only for the specimens in the stressing rate experiments. For all other specimens, this surface was unpolished. The tensile surface was polished until the opposing specimen surfaces were perfectly parallel to each other. This inner surface was then polished using a 600 grit, 1200 grit, and 1 μm aluminum paste sequence.

Figure 3.1 Specimen cut in direction parallel to the long axis of shell.

3.1.2 Water Storage

Each specimen was maintained in 100 ml of an aqueous solution for three weeks prior to fracture. Specimens were stored in one of five solutions: distilled deionized water, a pH 4.0 buffer solution, a pH 10.0 buffer solution, an artificial seawater solution, and natural seawater. The distilled deionized water was the standard solution and had a pH of 7.0. The two buffer solutions, pH 4.0 and pH 10.0 were unchanged during the storage period. The artificial seawater was prepared according to Kamat et al.[12]

The natural seawater was obtained from the Gulf of Mexico on the west coast of Florida and had a pH of 8.01. Twenty-four specimens were stored in each solution.

3.1.3 Protein Removal

Pieces of the *Strombus gigas* were powdered using a mortar and pestle. This powder was heated to 150°C for 24 h to remove any free water. Differential thermal scanning calimetry (DSC) and thermogravimetric/differential thermal analysis (TG/DTA) (TG/DSC/DTA Model 320, Seiko Instruments, Tokyo, Japan) were used to determine any changes in weight and kinetics as a function of increasing temperature. From these results a heat treatment schedule was designed to remove the proteinaceous matrix. A second run was performed to determine if the protein had been removed. Each powder was heated between 25°C and 400°C at 10°/min, while the weight, entropy and enthalpy were measured. The scans from these analyses are shown in Figures 3.2 and 3.3.

From these results, it was determined that protein could be removed at 200°C for 24 h. X-ray diffraction was then performed to assess if the crystal structure had changed from aragonite to any other polymorph of calcium carbonate.

3.2 Material Properties

3.2.1 Density

The densities of the shells were measured in two forms, powder and monolithic, and in three storage conditions: water, ambient atmosphere, and heat treated (200°C for 24 h). The densities were calculated by obtaining the mass and volume of each of the specimen. Each specimen was weighed using a precision balance (Model HL 52, Mettler Instruments Corp., Hightstown, NJ). The volume of each specimen was then determined using a helium pycnometer (Model MPY-1, Quantachrome Corp., Syosset, NY).

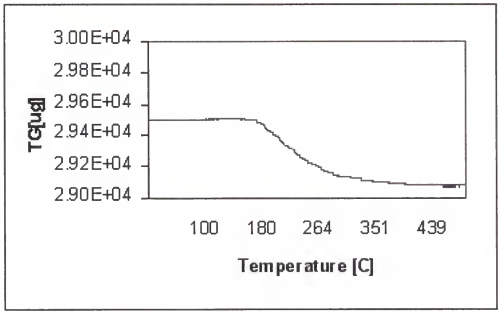

a) Heat treated at 120°C for 24 h

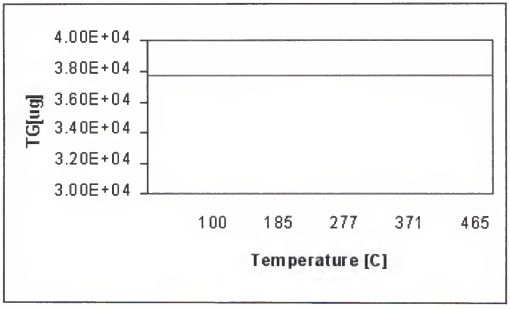

b) Heat treated at 200°C for 24 h

Figure 3.2 Thermogravimetric/differential thermal analysis (TG/DTA) graphs (a) prior to and (b) post heat treatment.

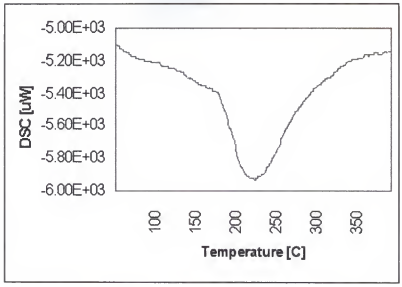

a) Heat treated at 120°C for 24 h

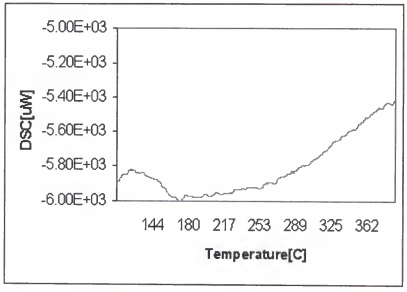

b) Heat treated at 200°C for 24 h

Figure 3.3 Differential scanning calorimetry (DSC) graphs (a) prior and (b) post heat treatment.

3.2.2 Hardness

The hardness was measured using a microhardness tester (Model MO Tukon Microhardness Tester, Wilson Instruments Inc., Binghamton, NY) using a Vickers diamond indenter. Prior to the indentation, the inner specimen surfaces were polished to a 1μm finish. The surface was determined using a 20x magnification and the load was released. The lengths of the Vickers diagonals were measured using a filar eyepiece in an optical microscope at a magnification of 40x. The hardness values were calculated using the equation

$$H = 2P \sin(\theta/2)/a^2 \tag{3.1}$$

where P is the indentation load, θ is 136 (the angle between the Vickers diamond faces), and a is the mean length of the diagonals.

Specimens were indented using five environmental conditions: (1) ambient atmosphere / room temperature; (2) deionized water / room temperature; (3) ambient atmospheric / 80°C; (4) deionized water / 80°C; and (5) ambient atmosphere / 4°C. For each condition five specimens were indented five times each in different locations for each load. Indentation loads of 0.10, 0.49, 4.9 and 19.6 N were used. The indentations were separated by over ten times the diagonal length to prevent overlap of the indent residual stress field.

3.2.3 Elastic Modulus and Poisson's Ratio

The elastic moduli and Poisson's ratio values were determined for 10 specimens of each of three conditions: (1) stored in deionized water; (2) stored in room air; and (3) heat treated at 200°C for 24 h. Segments of the shell taken from the three primary directions of each specimen were analyzed. In addition, four specimens from each group

were sliced between the inner and middle layer and measured to determine the elastic constants of the layers. An ultrasonic pulse apparatus (Ultima 5100, Nuson Inc., Boalsburg, PA) measured the velocity of sound through the specimen. Piezoelectric transducers of 5 MHz (SC 25-5 and WC 25-5, Ultran Laboratories, Inc., Boalsburg, PA) generated shear and longitudinal waves. The transducers were coupled to the specimen with honey (for shear waves) and glycerin (for longitudinal waves). An electronic delay was subtracted from each measurement to give the actual velocity of sound. From these values, the Poisson's ratios (ν) were calculated using the equation:

$$\nu = \frac{1 - 2(\frac{v_s}{v_l})^2}{2 - 2(\frac{v_s}{v_l})^2} \tag{3.2}$$

where v_l is the longitudinal velocity and v_s is the shear velocity. The Young's modulus was then calculated using the equation:

$$E = \frac{\rho v_l^2 (1+\nu)(1-2\nu)}{1-\nu} \tag{3.3}$$

where ρ is the density.

3.2.4 Crystal Phase Identification

X-ray diffraction analysis was performed to ensure that the crystal structure remained aragonite and had not converted to calcite following the removal of the proteinaceous phase. Specimens were analyzed prior to heat treatment, following the heat treatment determined by DSC/DTA, and following a heat treatment 100°C above the heat treatment temperatures. Shell specimens from each group were ground using a mortar and pestle and sieved with 325 mesh screen. The powders were mixed in amyl

acetate, which was mounted on a glass slide. This was analyzed employing an X-ray diffractometer (APD 3720, Philips Electronic Instruments Inc., Mahwah, NJ) using a $K_{I\alpha}$ Cu source. All scans were taken over 2θ range of 10° to 90° at 3°/min at a count rate of 1000 counts per minute.

3.3 Mechanical Property Determination

3.3.1 Flexure Strength

The flexure strength of all specimen groups was evaluated using 4-point flexure of non-indented specimen. The flexure experiments were performed on two universal testing machines. The stressing rate experiments were tested using a hydraulic Instron testing machine (Model 8511, Instron Corporation, Canton, MA) using a 200 lb. load cell, while all other flexure specimens were tested on a hydraulic Instron testing machine (Model 8700, Instron Corporation, Canton, MA) using a 10 kg load cell. All flexure specimens were performed using the same 4-point bend fixture with a 39 mm outer span and a 13 mm inner span. Figure 3.4 shows a diagram of the loading of a flexure specimen positioned in an articulating 4-point bend apparatus. All non-stressing rate specimen groups were tested at a crosshead speed of 0.1 mm/min under displacement control.

The stressing rate experiments were performed at rates of 0.02, 0.5, 20, and 500 MPa/s as a function of the total specimen thickness. The loading rate, $\dot{P}$ (N/s) was calculated using the equation:[45]

$$\dot{P} = \frac{4\dot{s}bd^2}{3L} \tag{3.4}$$

where $\dot{s}$ (MPa/s) is the stressing rate throughout the load span, L (mm) is the support span, b (mm) is the width of the specimen, and d (mm) is the thickness of the specimen.

The strengths of the specimens were calculated using three methods: simple beam theory, simple beam theory using the middle layer thickness, and laminate beam theory. First the flexure strength was calculated for simple beam theory according to the following equation:

$$\sigma_f = \frac{Mc}{I} \tag{3.5}$$

where c is the distance from the neutral axis, M is the moment corresponding to maximum loading, and I is the maximum load. Inserting these factors into Equation 3.5, the relation transforms to the following equation[46] for a loading span of one third of the support span (Figure 3.4):

$$\sigma_f = 3PL/4bd^2 \tag{3.6}$$

where σ_f is the maximum stress, P is the maximum load, and L, b, and d are defined by equation 3.4.

The simple beam theory using middle layer thickness, d, was calculated using equation 3.6. This method was derived by Currey[49], who hypothesized that the strength of the cross-lamellar structure is primarily a function of the middle section which carries the load. The middle layer thickness was determined using an optical microscope and filar eyepiece. Thickness was measured at the fracture surface after fracture (Figure 3.5).

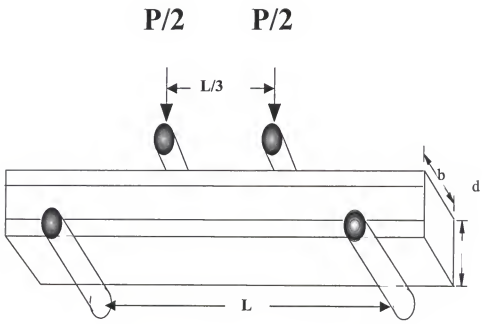

Figure 3.4 Four point loading configuration

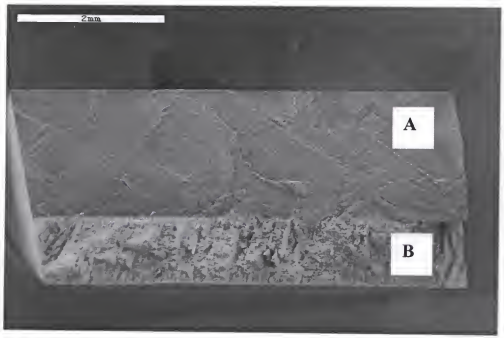

Figure 3.5 SEM micrograph showing fracture surface showing microstructural layers.

The flexure strength based on laminate beam theory[47-49] was calculated according to the equation

$$\sigma_f = E\frac{h}{2}\frac{M}{\overline{EI}} \tag{3.7}$$

where σ_f is the stress at fracture, E is the elastic modulus of the specimen, h is the thickness of the specimen, M is the bending moment, and $\overline{E}$ is the flexural rigidity. The flexural rigidity was calculated by the equation:

$$\overline{EI} = w\int_{i}^{i} E_L z_i dz \tag{3.8}$$

where $i = 2$ after the exterior layer had been removed by polishing, w is the specimen width, and E_L is the elastic modulus for the layer defined by z_i. The values of z_i are determined by their position relative to the neutral axis, where the neutral axis was determined by a transformation factor as described by Thompson.[55]

3.3.2 Work of Fracture

The work of fracture was calculated by integrating the area under the load-displacement curves and normalized using the cross-sectional area of the specimen. The strain for each specimen was determined by cross head displacement and calculated by the following relation for ASTM Standard D790-96a for a load span one third the support span:

$$D = 0.21rL^2 / d \tag{3.9}$$

where D is the midspan deflection (mm), r is the specimen strain, L is the support span and d is the depth of the beam. The cross-sectional area for each specimen was measured post fracture at the fracture plane.

3.3.3 Fracture Toughness

The fracture toughness was evaluated using a single edge-notched beam (SENB) method. This method was used to evaluate the toughness of the strong middle layer and the weaker inner layer of three groups of specimen: stored in deionized water, stored in air, and heat treated at 200°C for 24 h. Six groups were fabricated and a band saw (Model 850, South Bay Technology Inc., Temple City, CA 91780) was used to cut through the middle or inner layer, producing specimens with one layer completely cut through (Figure 3.6). The specimens were then stressed to fracture at a stressing rate of 0.1 mm/min and a load-displacement curve was recorded. After fracture, each specimen was viewed to ensure that the fracture occurred uniformly from the single edge precrack. All specimens in which failure occurred elsewhere were discarded. The depth of cut was viewed at a magnification of 20x under an optical microscope and measured using a filar eyepiece.

Using the information from above, the fracture toughness, K_{IC}, was calculated by the following equation[56]

$$K_{IC} = Y \frac{3PL}{bd^2} c^{1/2} \tag{3.10}$$

where P is the maximum stressing load, L is the length of the support span, b is the specimen width, d is the specimen thickness, c is the depth of cut or crack depth, and Y is a geometric variable calculated by the equation

$$Y = 1.99 - 2.47\left(\frac{c}{d}\right) + 12.97\left(\frac{c}{d}\right)^2 - 23.17\left(\frac{c}{d}\right)^3 + 24.8\left(\frac{c}{d}\right)^4 \tag{3.11}$$

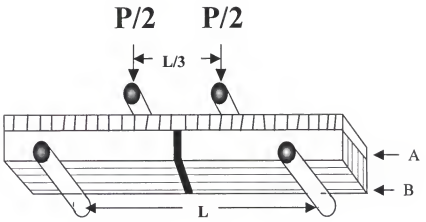

a) Test design for inner layer (A) fracture toughness K_{IC}

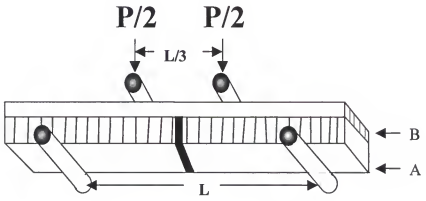

b) Test design for inner layer (B) fracture toughness K_{IC}

Figure 3.6 Single edge-notched beam configuration to determine fracture toughness of *Strombus gigas* for the (a) weaker inner layer and (b) stronger middle layer

3.4 Fractal Analysis

The fractal dimensions were determined at two levels of magnification, which correspond to the hierarchical structure of the conch shell. The optical microscope profiles were analyzed using the Richardson technique, described later, while the AFM produced a three-dimensional profile from which the fractal dimension was determined.

Since the structure of the two first order layers have such different fracture surfaces, both areas of the specimen were analyzed using both the modified slit island technique (large scale) and the box counting technique (fine scale). The atomic force microscope was used in the study to determine if any relationship exists between the weaker inner layer fracture surface and stronger middle layer fracture surface on the same specimen, along with their specific hierarchical fracture levels.

3.4.1 Modified Slit Island Method

The first two steps of obtaining the fractal dimension using the optical microscope dealt with creating an epoxy resin replica of the fracture surface. The fracture surface was cleaned ultrasonically in ethanol. Subsequently, it was carefully coated with a thin layer of impression material, a low viscosity polyvinylsiloxane (Kerr Manufacturing Co., Romulus, MI).

This initial thin layer was applied to the fracture surface to reduce void formation between the fracture surface and the impression material. The specimen was then inverted into a mold containing additional impression material. The impression was allowed to set for 30 min and then removed to produce a negative replica of the fracture surface. The negative replica was degassed at room temperature for 12 h.

An epoxy resin (Leco Epoxide Resin) was mixed and poured into the impression mold. It was inspected to ensure that no bubbles had formed. The filled mold was placed in a curing oven at 60°C for 1 h. The cured epoxy resin was then separated from the impression. If any surface defects were observed, the replica was discarded, and another replica was produced. The mold could be used up to three times before its surface integrity was lost. The replica was then sputter coated with gold-palladium for 8 min. The replica was covered with additional epoxy to enhance the contrast at the fracture surface when polished.

The replica was polished parallel to the fracture surface using 1200 grit silicon carbide abrasive until the initial portion of the coated specimen started to reveal the appearance of boundaries or islands from the fracture surface at different elevations. Once a desired location on the fracture surface is revealed, the specimen was polished using 1 μm alumina abrasive for 3 min to enhance edge resolution.

The polished replica was viewed under an optical microscope at a magnification of 400x. The gold-palladium/epoxy coastline was photographed in sections. From these photographs, a montage was constructed using seven to 10 photographs.

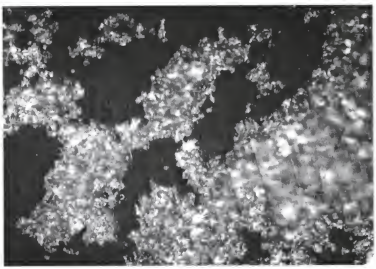

Figure 3.7 Optical micrograph (400x) showing the coastline of a polished replica.

The coastlines of the conch specimen from the optical microscope were analyzed using the Richardson technique. The coastlines of each montage were measured using a series of measurement ruler lengths. Each total length measured was recorded and then plotted on the natural log of the total line length versus the natural log of the measurement length graph.

The slope of the line generated (Figure 3.8) is equal to one minus the fractal dimension (1-D) as calculated by the Richardson equation:

$$L = constant \times S^{1-D} \qquad (3.12)$$

where L is the length of the line that was measured, S is the measuring unit being used, D is the fractal dimension and 1-D = D*, the fractal dimensional increment.

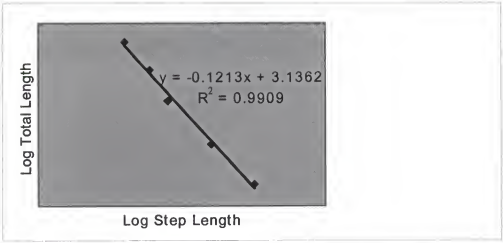

Figure 3.8 Plot of log of Total Length versus log of Step Length. The slope giving the negative value of the fractal dimensional increment.

3.4.2 Box Counting Technique Using the Atomic Force Microscope

The second method was performed using the atomic force microscope in the contact mode. The AFM tip slowly approached the surface to be analyzed where atomic forces develop between the atomically sharp tip and the fracture surface. As the tip scans across the profile area (5 μm by 5 μm), a depth profile of the fracture surface is created. Five scans were made from each specimen fracture surface.

The fractal dimension was then calculated using a pre-programmed box counting algorithm where the end points were selected with respect to the slope of the line for the size counts as shown in Figure 3.8.

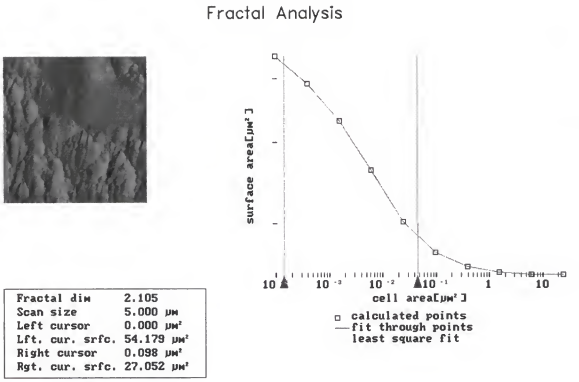

Figure 3.9 A representative image of the fractal dimension obtained using the atomic force microscope.

CHAPTER 4
RESULTS AND DISCUSSION

In the following sections, the data obtained for the physical properties, mechanical analysis, and fractal measurements of the *Strombus gigas* are presented primarily in graphical format (Sections 4.1, 4.2, and 4.3) with a discussion of the relevance of each finding included. The data for individual specimens are listed in the Appendix.

4.1 Physical Properties Analysis

4.1.1 Density

The mean apparent density values for the *Strombus gigas* in monolithic and powder form stored in air, stored in water for two weeks, and heat treated at 200°C for 24 h are summarized in Figure 4.1. The bulk density of the monolithic specimen ranged from 2.788 ± 0.008 g/cm^3 for heat treated specimen to 2.906 ± 0.011 g/cm^3 for the specimen stored in deionized water. The powdered specimen density ranged 2.876 ± 0.006 g/cm^3 for the heat treated specimen to 3.123 ± 0.010 g/cm^3 for the powdered specimen stored in air. One-way ANOVA showed that density increased with the presence protein and water in all cases except between the powdered specimen stored in air and the powdered specimen in water for which any differences were statistically insignificant. In all cases, the density of the powder groups was greater than that of the corresponding monolith groups. The theoretical density for aragonite is 2.9 g/cm^3 [57] that is lower than that of the wet powdered specimens. The probable explanation for this fact is that the biological aragonite contains some magnesium impurities in aragonite lattice

positions instead of calcium. The monoliths have an average porosity of six percent calculated from the ratio of the density of the monolith specimens to the density of the powder specimens with the air specimens showing the greatest difference between monolith and powder. This porosity allows channels for the movement of water through the cross-lamellar structure.

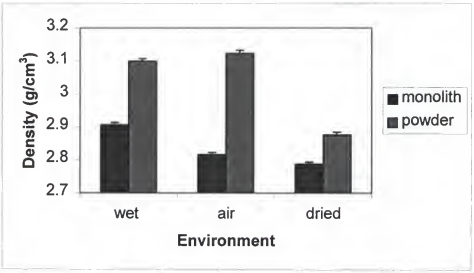

Figure 4.1 Density of *Strombus gigas* as a function of environment in monolithic and powder form.

4.1.2 Hardness

The mean hardness values for five environmental/temperature conditions at five loads are summarized in Figure 4.2. The five conditions were air/room temperature (25°C), deionized water/room temperature, air/80°, deionized water/80°C, and air/4°C. The five loads were 0.10, 0.49, 0.98, 4.9 and 19.6 N. One-way ANOVA showed that the measured Vickers hardness increased with increasing load between the 0.10 N and all the other measurements. In all environments the hardness gradually increased at the 0.10 N load up to the 0.98 N load. This increase in hardness is opposite to the usual response in ceramic

materials where the hardness decreases with increasing load. This phenomenon appears to occur because of a crushing zone (Figure 4.3) beneath the indentation so that the load is distributed over a greater area than is recorded from the indentation, producing a smaller indentation than would be predicted. After the 0.98 N indent load, the hardness values displayed a general plateau for the room temperature specimen in air and water. A slight increase in Vickers Hardness is still present for the other environments.

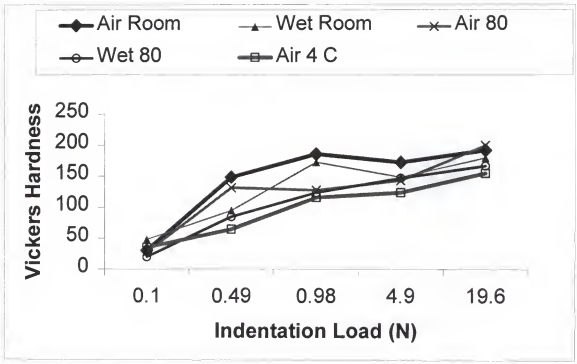

Figure 4.2 Vickers indent hardness as a function of indent load for five environment/temperature conditions.

4.1.3 Elastic Modulus and Poisson's Ratio

The elastic modulus was measured in the three primary directions for the *Strombus gigas* for all layers and only the middle layer. The specimens were measured in air and then again after being stored in water for 24 h at room temperature. Figures 4.4 and 4.5 show these values. Measurements for the heat treatment specimens could not be obtained using the ultrasonic technique.

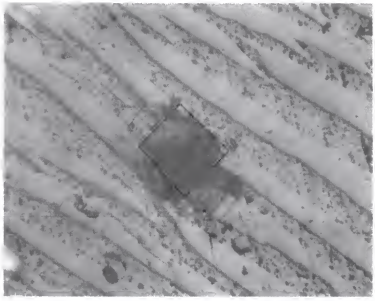

a) optical micrograph (100x) showing indent with respect to microstructure. Dotted line outlining indent.

b) optical micrograph (400x) showing crushing zone around indentation. Dotted line outlining indent.

Figure 4.3 Optical micrograph of indentation with respect to a) shell microstructure (100x) and b) crush zone (400x) around the indentation

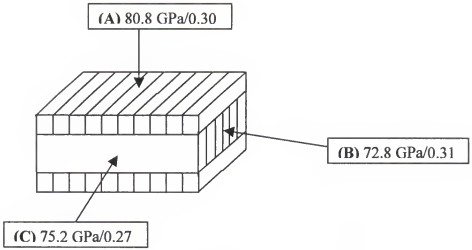

a) stored in air

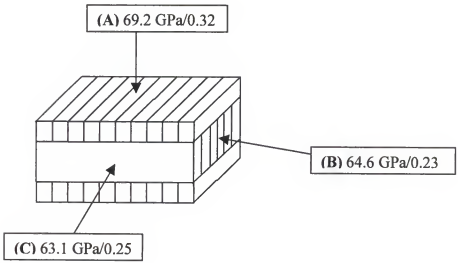

b) stored in deionized water

Figure 4.4 Elastic moduli and Poisson's ratio values for full thickness *Strombus gigas* specimens obtained by ultrasonic measurements in air (a) and in water (b).

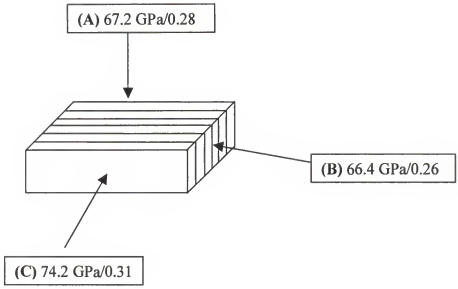

a) stored in air

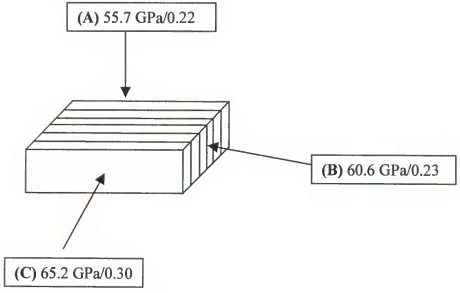

b) stored in deionized water

Figure 4.5 Elastic moduli and Poisson's ratio values for middle layer of *Strombus gigas* specimens obtained by ultrasonic measurements in air (a) and in water (b).

For both cases, the middle layer specimen and full thickness specimen, the elastic moduli decrease approximately 10 GPa after being stored in deionized water. This phenomenon is consistent with previous work done by Jackson et al.[6] for *Pinctada* Nacre. They observed a decrease from 70 GPa for "dry" specimens to 60 GPa for wet specimens where the Young's modulus was obtained from stress-strain plots. A lesser difference in elastic moduli, of about 4 GPa, was observed by Currey[4] between the downward, (A) direction, and the side, (B) direction. The difference between these directions appears to be greater for the cross-lamellar *Strombus gigas*, about 10 GPa. For measurements on the middle layer, the elastic modulus values are slightly lower (highest of 74.2 GPa for air and 65.2GPa for storage in water). The difference between the multiple layer and single layer values may be due to the ultrasonic measurement technique. The technique is sensitive to specimen shape. If one direction becomes too long or thin in comparison to the others, the ultrasonic waves can have loss which lowers the calculated values. The minimum width of the across directions is determined by the size of the transducers used, about 5 mm while the thickness of the layers are about 2-3 mm. The optimal shape for obtaining a measurement is a cube. The highest and lowest values obtained for the middle layer were used in composite strength calculations.

4.1.4 Crystal Structure

X ray diffraction was performed on three specimens to determine if the aragonite crystal structure remained after heat treatment. The spectra from each specimen was compared to JC-PDS records. Figure 4.6 shows the results of the powdered specimen prior to any heat treatment and had been stored in air. Figure 4.7 shows the spectra for the powder after heat treatment at 200°C for 24 h.

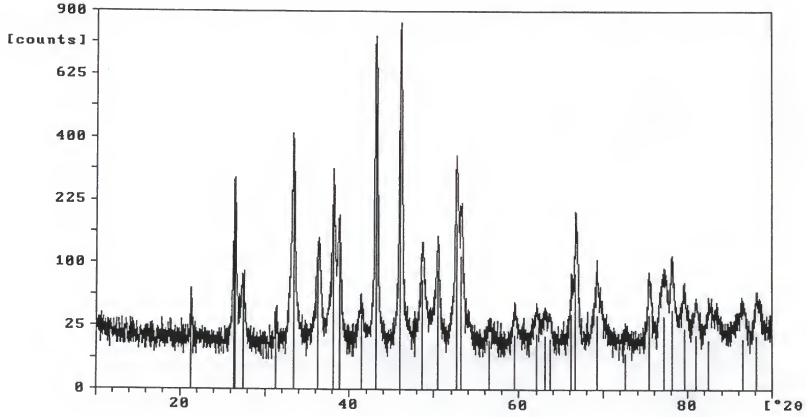

Figure 4.6 X-ray diffraction spectra for *Strombus gigas* powder stored in air. Aragonite crystal structure is only phase phase.

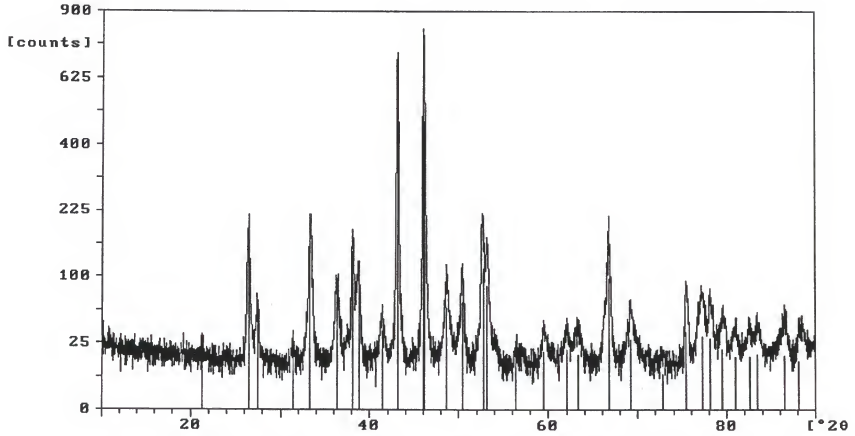

Figure 4.7 X-ray diffraction spectra for *Strombus gigas* powder heat treated at 200°C for 24 h. Aragonite crystal structure is only phase phase.

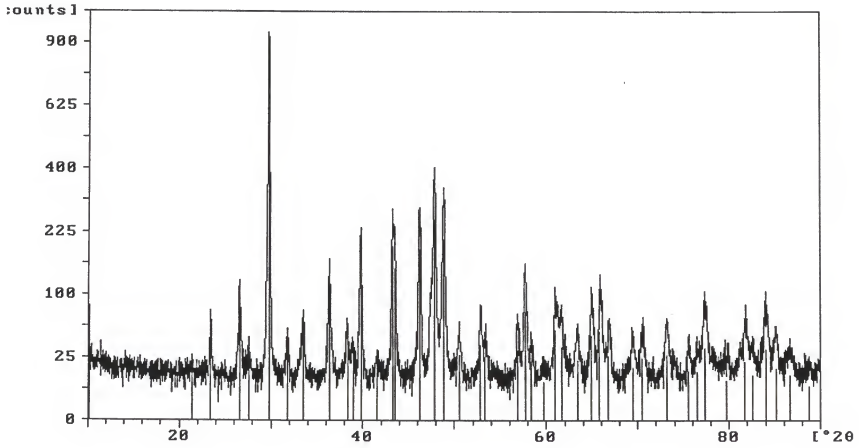

Figure 4.8 X-ray diffraction spectra for *Strombus gigas* powder heat treated at 300°C for 24 h. Calcite crystal structure is primary phase.

The three notable peaks for an aragonite specimen are at d-values of 1.98, 3.26, and 3.39 that are present at high intensities in Figure 4.6 and Figure 4.7. No peaks representing calcite or vaterite are present in either scan. Figure 4.8 shows the x-ray scan of a powdered specimen heat treated at 300°C for 24 h. The highest intensity peaks for this scan do not align with those for the aragonite crystal like the primary peaks in Figures 4.6 and 4.7. Those peaks are still present to a much lower intensity, but the highest intensity peaks correspond to calcite peaks at d-values of 3.00, 1.88, and 1.94. Many double peaks appear in all the specimens, which may be an indication of twinning, which is present in the *Strombus gigas* structure, or due to internal stresses.

4.2 Mechanical Properties Analysis

4.2.1 Strength

The strength values calculated by the linear beam model (LB), the linear beam model using middle layer thickness (ML), and the composite laminate beam model f or flexure specimen stored in air (AIR), stored in deionized water (DI), and heat treated at 200°C for 24 h (burnout) are displayed in Figure 4.8. The middle layer model (ML) was classified by Currey and Kohn[5] for analyzing the cross lamellar structure. They determined that the strength of the cross lamellar composite was due primarily to the middle layer and then calculated strength values using the linear beam model but with the thickness value being the middle layer thickness. When they calculated the strengths using this method they obtained a much narrower distribution with much less scatter and concluded that their assumption was valid. The mean strength values for this study ranged from 17.9 MPa (burnout-linear beam) to 249.2 MPa (deionized water middle layer). The means calculated using the linear beam model and the uncracked

thickness (middle layer) model correspond well with previous values reported by Kuhn-Spearing[11] for both the groups in air and water, but that group did not use laminate composite theory to calculate the strength of the *Strombus gigas*.

The mean flexure strength calculated using the composite laminate theory was between the mean flexure strengths of the linear beam model and the middle layer model for all conditions. One-way ANOVA showed that the mean flexure strength of specimens stored in air were statistically greater than the mean flexure strength of the heat treated specimen group while the mean flexure strength of the specimen stored in deionized water were statistically greater than both of the air and burnout groups. The ordering of the three groups is due to the presence of protein and water in the structure and the increased plasticity in the specimen from the addition of the water and protein to the structure.

The mean strength values for the heat treated group display a 5- to 10-time increase compared with that of geologically produced monolithic $CaCO_3$.[58] This increase in strength is due to the cross-lamellar structure in the absence of the protein matrix producing a fracture similar to that for a weakly bonded brittle/brittle composite. The mean strength values for the group in air were 3 to 6 times higher than that of the heat treated group due to the protein holding the structure together. In this situation, the presence of the protein changes the fracture to act like a strongly bonded brittle/ductile composite. Finally, only an approximately 50 percent increase is seen with the introduction of water into the structure, though the fracture does appear more like that of a weakly bonded brittle/ductile composite.

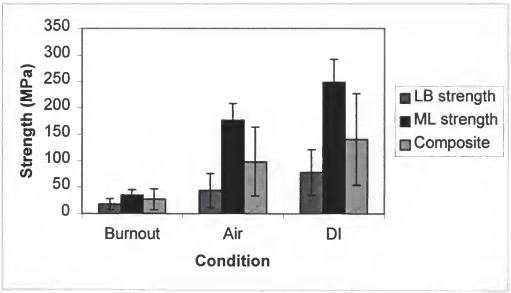

Figure 4.9 Mean strength for *Strombus gigas* specimens stored in air, stored in deionized water, and heat treated at 200 C for 24 h calculated using linear beam analysis, linear beam analysis using middle layer thickness and composite analysis.

Figure 4.10 shows the mean strength calculated using linear beam analysis, middle layer linear beam analysis, and composite analysis for four-point flexure specimens stored in six environments at room temperature: air, deionized water, natural seawater, pH4 buffer solution, pH10 buffer solution, and an artificial seawater solution. Duncan's multiple range test revealed a significant difference between the flexure specimen stored in air and the other groups at $\alpha = .05$, but no significant difference was determined among any of the other groups. These data demonstrate that water is the primary strengthening influence, and that ion concentration and solution pH did not have a significant effect on the strength of the flexure specimen. This is not to state that the solution did not affect the specimen because some precipitation occurred in the pH 4 buffer solution. In spite of the precipitation, the mean strength of the pH 4 group was not

statistically different in strength when compared to the other groups stored in an aqueous solution.

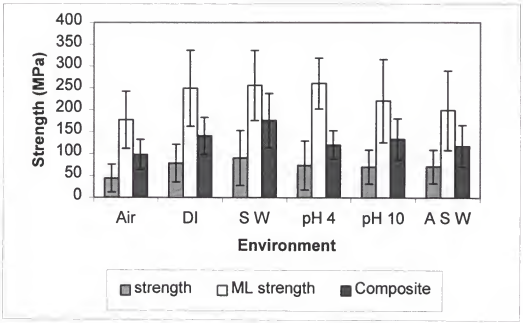

Figure 4.10 Mean strength values calculated using linear beam analysis, middle layer linear beam analysis, and composite analysis, stored in six environments: air (Air), deionized water (DI), natural seawater (SW), pH4 buffer solution (pH4), pH10 buffer solution (pH10), and artificial seawater solution (ASW).

Figure 4.11 shows the mean flexure strength for the *Strombus gigas* as a function of stressing rate. The strength values were calculated using both the linear beam model and the middle layer model. Specimens were stored in air or stored for two weeks in deionized water prior to fracture. One-way ANOVA did not determine a statistical difference for the linear beam model between specimens stored in air or in deionized water, though the largest difference in mean values was at a stressing rate of 0.02 MPa/s. For the middle layer model, the mean strength of the specimens stored in water was statistically different than the specimen stored in air and fractured at a stressing rate of 0.02 MPa/s while no difference was determined for the other stressing rates.

Using the middle layer model, the specimens stored in air generally increased with increasing stressing rate from a mean strength of 125 MPa at a stressing rate of 0.02 MPa/s to a strength of 201 MPa at a stressing rate of 500 MPa/s. The specimens stored in deionized water decreased with increasing stressing rate, though, for strength values calculated using the middle layer model. The mean strength values decreased from 253 MPa for a stressing rate of 0.02 MPa/s to 208 MPa for a stressing rate of 500 MPa/s.

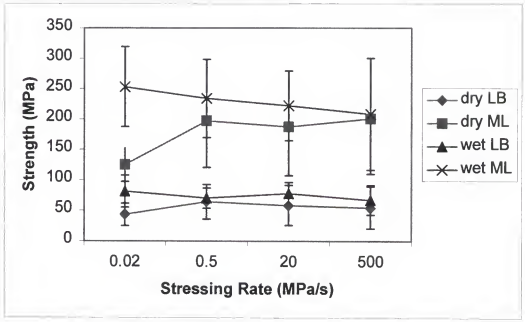

Figure 4.11 Mean strength values calculated by linear beam (LB) and middle layer (ML) linear beam as a function of increasing stressing rate.

4.2.2 Fracture Toughness

The fracture toughness was determined for the inner layer and middle layer of the *Strombus gigas* for three conditions: stored in air, stored in deionized water for two weeks prior to fracture, and heat treated at 200°C for 24 h. Figure 4.12 displays the mean fracture toughness values for these conditions. In all cases, the mean fracture toughness

of the middle layer is statistically greater than the mean fracture toughness of the corresponding inner layer. Using one-way ANOVA, the mean values for the specimens stored in water and stored in air are statistically different than the values for the heat treated group, but no difference is found between the air-stored or water-stored groups for the inner or middle layer groups. The fracture toughness values are slightly higher than the values previously published by Kamat et. al.[12] for the fracture toughness values determined by the single edge notch beam method for examining the weak inner layer and the stronger middle layer stored in either air and deionized water. The heat treated group displayed a mean fracture toughness value for the inner layer (0.42 MPa-m $^{1/2}$) greater than the fracture toughness of non-biogenic aragonite (0.25 MPa-m $^{1/2}$).

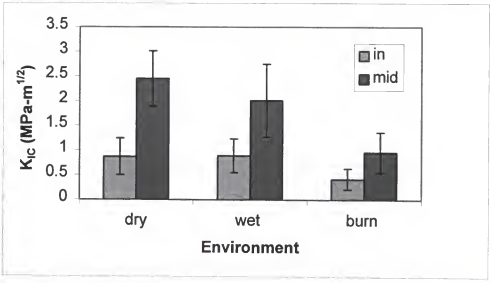

Figure 4.12 Mean toughness values determined using single-edge notch beam equation for three conditions: stored in air, stored in water, and heat treated at 200° for 24 h.

4.2.3 Work of Fracture

The work of fracture was determined as the area under the load displacement plot normalized by the cross-sectional area of each specimen at the fracture site. Figures 4.13 and 4.14 show the work of fracture as a function of environment and solution for several four-point flexure groups. In Figure 4.13, the means of all the groups are statistically different. The group stored in deionized water displayed a twenty-fold increase in work of fracture compared with the heat treated group (0.59 kJ/m^2 to 11.25 kJ/m^2) and a two-fold increase in work of fracture (4.76 kJ/m^2 to 11.25 kJ/m^2) compared with the group stored in air, indicating that the presence of the protein in the structure caused an increase in the work of fracture by approximately two times. In Figure 4.14, one-way ANOVA determined no statistically significant difference in mean work of fracture was observed among any of the groups stored in an aqueous solution prior to fracture, indicating that the ions present have little affect on the work of fracture, though all of these groups were greater than the group stored in air prior to fracture.

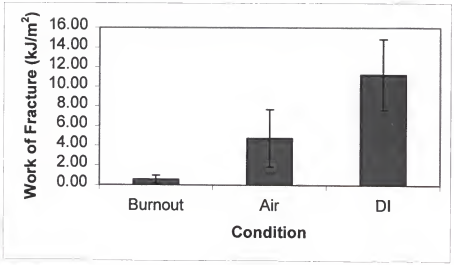

Figure 4.13 Work of fracture for specimens stored in air, deionized water and heat treated at 200°C for 24 h.

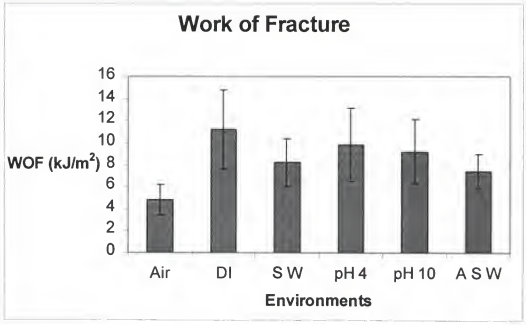

Figure 4.14 Work of fracture (WOF) for specimen stored in six environments: air (Air), deionized water (DI), natural seawater (SW), pH4 buffer solution (pH4), pH10 buffer solution (pH10), and artificial seawater solution (ASW).

Figure 4.15 shows the work of fracture as a function of stressing rate for the specimen groups stored in air and stored in water. For all stressing rates, the mean value of the work of fracture of the water group was statistically greater than the mean value of the work of facture for the specimen stored in air. The work of fracture increased from 2.45 kJ/m^2 for a stressing rate of 0.02 MPa/s to 4.05 kJ/m^2 for a stressing rate of 500 MPa/s. The group stored in water had a decreasing work of fracture with increasing stressing rate and ranged from 7.95 kJ/m^2 for 500 MPa/s to 11.83 kJ/m^2 for 0.5 MPa/s. The probable mechanisms for these trends will be discussed later on.

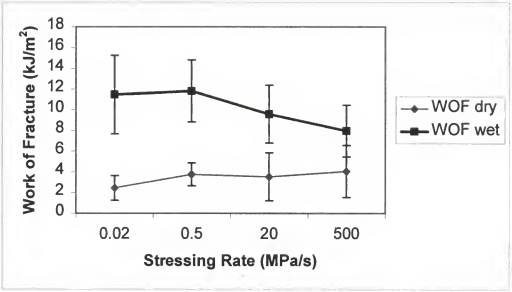

Figure 4.15 Work of fracture as a function of stressing rate for groups stored in air and in deionized water.

4.2.4 Fracture

The fracture surfaces of the *Strombus gigas* demonstrate two macroscopic hierarchical levels of fracture as shown in Figure 4.16. It can be seen that the inner layer (layer A in Figure 4.16) is relatively smoother than the middle layer (layer B in Figure 4.16). The inner layer (A) was always on tensile surface during four-point flexure. The relatively smooth channels are stressed and open up in many planes from the tensile surface much like microcracking and produce many channel cracks that toughen the biological composite. The introduction of these channel cracks between the first order lamella of the inner layer (A) causes the central axis of the composite to shift down into the middle layer. Figure 4.17 shows the inner layer (A) at a higher magnification displaying the edges of some of the second order lamella. Fracture occurs between this second order structure easily, propagating between layers, except for some crack branching and arrest shown by the white arrows in Figure 4.17, until the cracks reaches

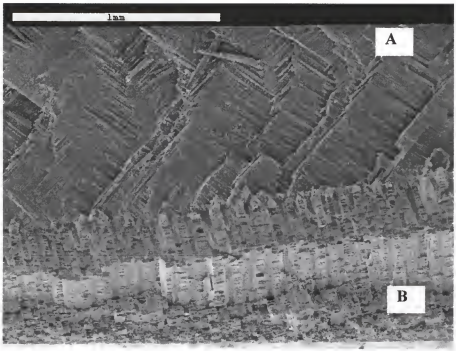

Figure 4.16 SEM micrograph of the fracture surface of a *Strombus gigas* at a magnification of 20x displaying the two distinct fracture surfaces.

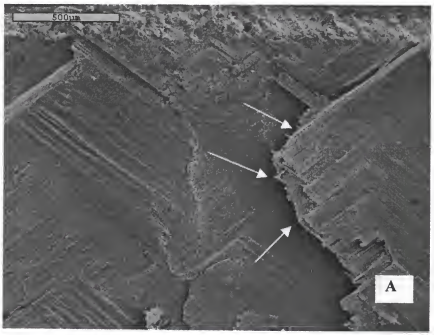

Figure 4.17 SEM micrograph of the inner layer of a fracture surface of a *Strombus gigas* at a magnification of 50x.

the tougher middle layer. Some delamination occurs between the inner and middle layers (A and B), where the propagating crack arrests at the interface, and then reinitiates once the local stress is great enough to propagate through the tougher middle layer (B). The delamination toughening mechanism greatly increases the work of fracture. Many of the cracks in the structure are produced while the crack is arrested at the interface between layers (A) and (B). Much energy is consumed to form and propagate these cracks to the interface between the two layers.

The propagation of a single crack through the middle layer occurs at a much higher stress level than the formation of the channel cracks in the inner layer. More toughening mechanisms are seen in the tougher middle layer (B) that are not seen in the inner layer (A). Figure 4.18 demonstrates the excessive amount of crack deflection, shown by the white arrows, and "fiber" pullout, shown in the white circles. Much energy is used to propagate a crack through this tough layer because of these two mechanisms. The structure of this middle layer causes the crack to travel in steps in a zigzag motion. The cracks must follow along this very tortuous path traversing the interlamellar boundaries until they connect and cut through a lamella to proceed further.

Looking at the end of the lamella in the middle layer at a higher magnification, Figure 4.19, it can be seen how the crack must travel complete around the lamella at each hierarchical level, producing a feature very similar to fiber pull out in advanced ceramic-ceramic composites. It can be seen from these observations and from previous work [7,8,9,11,12,13] that the *Strombus gigas* uses many toughening mechanisms: microcracking between the third order lamella and shown b the channel cracks; crack blunting between the first order lamella, crack reinitiation between the crystals in both the inner and middle

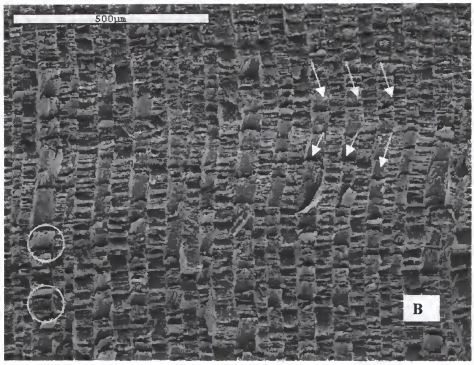

Figure 4.18 SEM micrograph of the tough middle layer of a fracture surface of a *Strombus gigas* at a magnification of 50x.

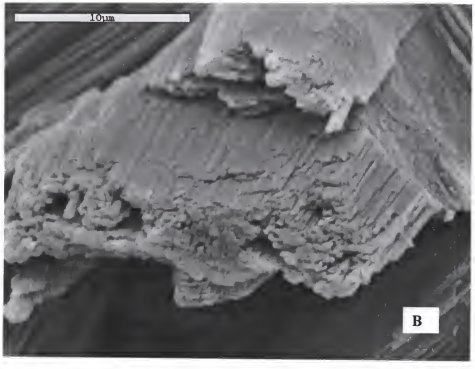

Figure 4.19 SEM micrograph of a second order lamella of *Strombus gigas* at a magnification of 2500x showing fracture across the third order lamellae

layers, delamination between the inner and middle layer, crack deflection primarily in the tougher middle layer, and fiber pull out of the crystals in the middle layer, to cause a remarkable increase in the energy, as measured by the work of fracture, to propagate a crack through the multilevel designed structure producing a very tortuous crack path

Figure 2.2 is a summary of the mechanical behavior of non-transformation toughened laminates based on the structure and interface between the laminates. Looking at the stress strain diagrams of the *Strombus gigas* in the three conditions in this study: heat treated to remove the proteinaceous matrix, stored in air and stored in water. Many similarities can be seen between them and the models in Figure 2.2.

The stress-strain curve for the specimen heat treated to remove the protein matrix shows a brittle type of failure (Figure 4.20a). After the initial alignment of the specimen in the four point loading fixture, the stress increases almost linearly until failure occurs at a low strain and stress. This behavior is similar to a brittle-brittle laminate with weak interfaces. Since the protein is absent, the interfaces will be very poorly bonded between the crystals. Evidence of microcracking and interface delamination are present on the fracture surface as predicted by the model and occur along the weak interfaces. Though this type of composite produces improved properties over the monolith, which this condition does, the limiting factor is the weakness of the interfaces.

The stress-strain curve of the group stored in air (Figure 4.20b) shows a much higher toughness and strength than the heat treated group. This group is best modeled like the brittle-ductile composite with strong interfaces. The model predicts that crack arrest, crack reinitiation, limited bridging and crack tip blunting will be present.

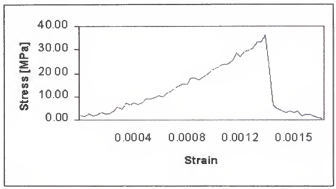

a) heat treated at 200°C for 24 h

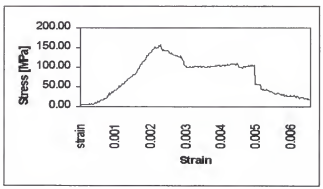

b) stored in air

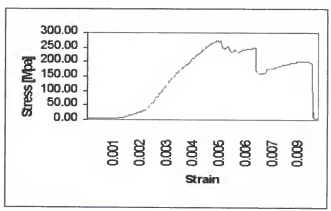

c) stored in deionized water

Figure 4.20 Representative stress-strain diagrams for *Strombus gigas* for three conditions.

Evidence of all of these mechanisms is present in the group stored in air. The strain at failure is much higher than that of a non-biogenic aragonite or the heat-treated group.

The stress-strain curve of the group stored in deionized water (Figure 4.20c) shows a much highest toughness and strength of the three groups. The stress-strain diagram is best modeled by a brittle-ductile laminate with weak interfaces. This model has many toughening mechanisms such as crack arrest, interface delamination, interface friction, ductile bridging, ductile yielding, crack tip blunting and crack reinitiation. Evidence of all of these mechanisms are seen on the fracture surfaces of fractured *Strombus gigas* specimens stored in water[8,11,12,13]. In Figure 4.21, the crack can be seen going into the cross lamellar structure of the *Strombus gigas* but not propagating completely through showing signs of crack blunting, reinitiation and interfacial friction. Figure 4.22 shows the stretching of many strands of protein demonstrating ductile bridging between the crystals, while Figure 4.23 shows the ductile yielding of one strand of protein that is still well bonded to the crystal. Figure 4.24 shows one of the many examples of interfacial delamination and crack arrest between the weaker inner layer (A) and the stronger middle layer (B). These mechanisms are all present in the groups stored in water which indicate a composite which acts like a brittle / ductile composite with a weak interface but is actually strongly bonded.

4.2.5 Water

In specimens stored in air, no evidence of the role of the protein matrix in the fracture process is not exhibited in this study. No visible sign of the protein was seen on any fracture surface of the groups stored in air while the protein is visible in all aqueous groups. The mechanical property values of strength and work of fracture were

significantly lower for the groups stored in air. Finally the specimen stored in aqueous solutions demonstrated a much greater deflection, higher strain to failure, and a lower elastic modulus. Evidently for the specimen groups stored in air, all toughening mechanisms are due to the increased tortuosity of the crack path and increased fracture surface area produced by the hierarchical structure of the conch shell. For the specimen stored in water though, the protein matrix appears to be pervasive on the fracture surface of the *Strombus gigas* as seen in Figures 4.21-4.23. The proteinaceous matrix can be seen on both first order fracture surfaces. It connects the crystals in the weak inner layer (Figure 4.22) and appears to be well bonded (Figure 4.23).

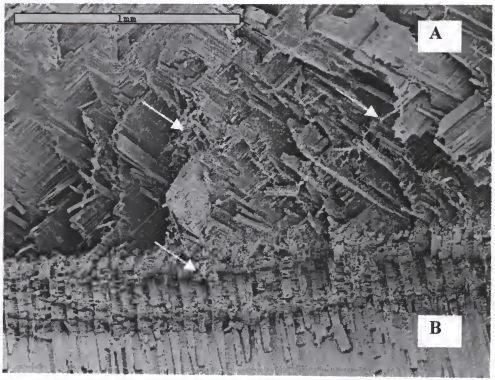

Figure 4.21 SEM micrograph showing both first order lamella of *Strombus gigas* stored in deionized water prior to fracture at a magnification of 20x. The presence of the proteinaceous matrix is pervasive. Arrows show a few examples of proteins present.

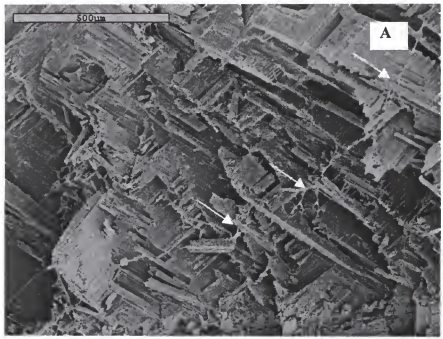

Figure 4.22 SEM micrograph of a second order lamella of the inner layer (A) of the *Strombus gigas* at a magnification of 50x shows the interconnecting protein. Arrows show interconnecting proteins.

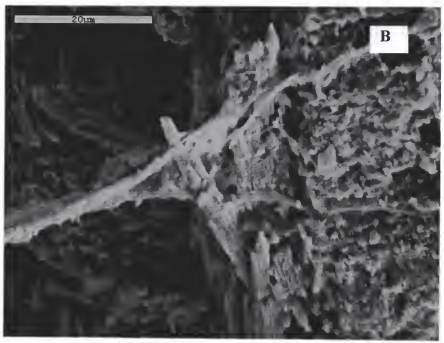

Figure 4.23 SEM micrograph showing the strong bonding of the protein with the aragonite crystals of *Strombus gigas* at a magnification of 2000x.

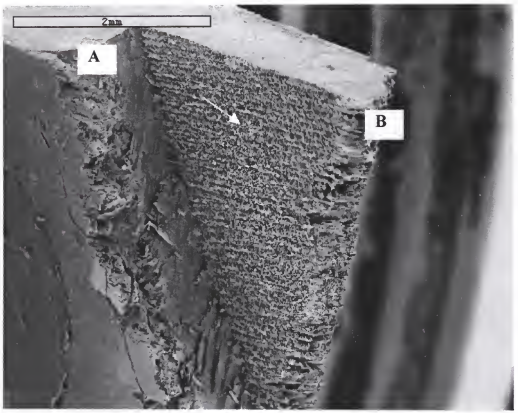

Figure 4.24 SEM micrograph showing the presence of the protein on the interface, denoted by the white arrow, between the inner (A) and middle (B) layers of *Strombus gigas* at a magnification of 20x.

Figure 4.24 shows the presence of the protein matrix at the interface between the first order lamella and the occurrence of delamination. This delamination requires a greater amount of energy to propagate a crack along the interface between the inner and middle layers than if no bonding or weak bonding exists between the two layers and then more energy is needed to reinitiate the crack through the middle layer (B).

Figures 4.25 and 4.26 show how the protein matrix is organized and how it is covers the interface between the inner and middle layers. Notice that the protein matrix forms an almost cell-like structure in an almost regular repeatable pattern indicating that the protein encompasses the crystal structure. The protein has been shown to be present

on all hierarchical levels of the *Strombus gigas* cross lamellar structure.[59] This repeating pattern suggests that the protein could be the template for the crystals to grow. The strong bonding between the crystal and protein along with the viscoelastic nature of the protein produces increased mechanical properties over the increases from the composite structure alone.

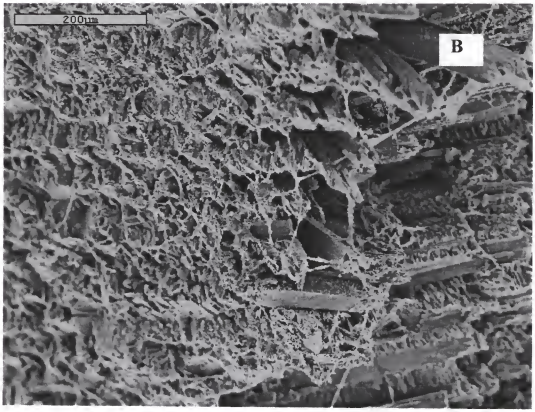

Figure 4.25 SEM micrograph showing the high organization of protein matrix with the aragonite crystals of *Strombus gigas* at a magnification of 200x

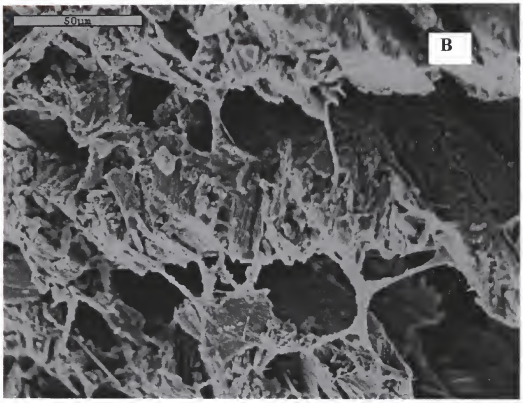

Figure 4.26 SEM micrograph showing the strong bonding of the protein with the aragonite crystals of *Strombus gigas* at a magnification of 800x

The effect of water on the mechanical properties of the *Strombus gigas* can be seen best by the effect of the work of fracture as a function of stressing rate. Figures 4.27 (a-d) show representative stress strain plots for specimen stored in air prior to fracture. As noted in Figure 4.15, the work of fracture increased with the specimen stored in air. Menig et al.[13] also demonstrated the same increase with stressing rate for two groups of *Strombus gigas* loaded in compression.

The increase of work of fracture with increasing stressing rate for the *Strombus gigas* can be explained by Caler and Carter's model[60] for bone damage, another ceramic-polymer composite with a large amount of ceramic (mineral) content. The model makes a prediction about monotonic tensile fractures. It predicts that bone or a brittle ceramic

composite will accumulate damage over time when stressed and that fracture will occur when a certain amount of damage has occurred as a function of stress level and time at the stress level. Therefore at the lower stressing rates, more time is allowed for damage to accumulate at each stress level than would be available at higher stressing rates. This phenomenon appears be true for the *Strombus gigas*. The higher stressing rate specimens reach greater strain values than the smaller stressing rate groups (Figures 4.27 a-d), therefore producing higher work of fracture values. Thus, the work of fracture and the strength values increase with increased stressing rates for the Strombus gigas tested in air.

In the presence of water, the work of fracture increases with decreasing stressing rate which is opposite to the trend of the group stored in air. The increase of work in fracture with decreasing stressing rate appears to be due to the presence of the protein-water interaction as suggested in the previous micrographs. The viscoelastic component of these proteins in the aqueous solutions allows for more deformation in the form of a greater strain to failure, causing more energy to be used before fracture occurs. The presence of water causes the flexural specimen to reach greater strains than the specimen stored in air. These strains are in some cases twice the values reached for the corresponding stressing rate specimens stored in air. The strains also increase with a decreasing stressing rate (Figures 4.28 a-d). The strong bonding between the crystals and the proteins allows the proteins to deform at greater strains before either breaking of the protein occurs or the protein debonds from the crystal producing a greater specimen deformation before fracture.

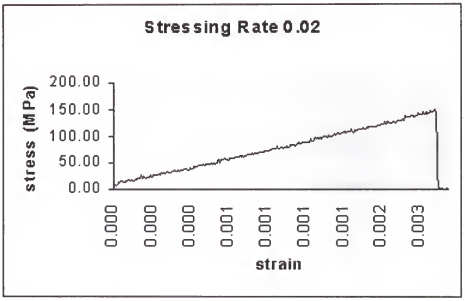

a) stressing rate of 0.02 MPa/s

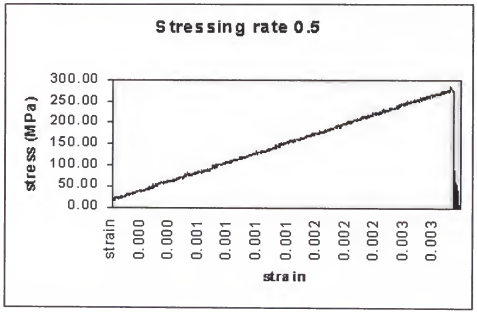

b) stressing rate of 0.5 MPa/s

Figure 4.27 Representative stress-strain plots for stressing rate groups stored in air

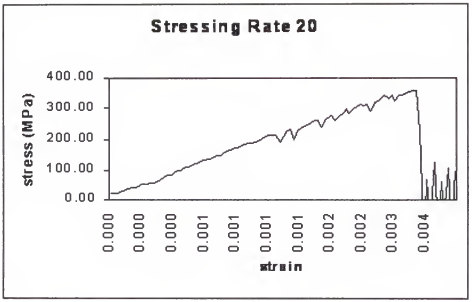

c) stressing rate of 20 MPa/s

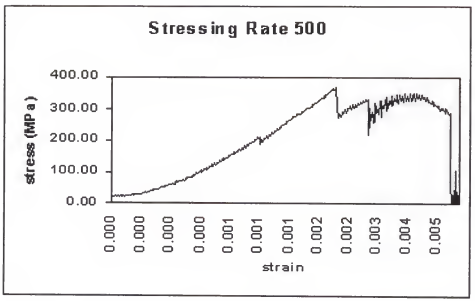

d) stressing rate of 500 MPa/s

Figure 4.27 Representative stress-strain plots for stressing rate groups stored in air

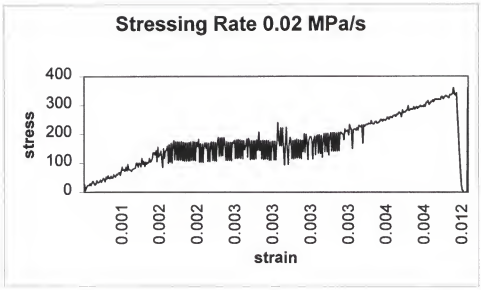

a) stressing rate of 0.02 MPa/s

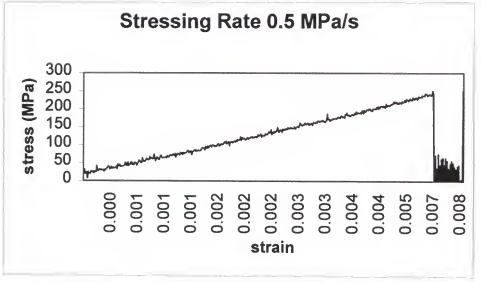

b) stressing rate of 0.5 MPa/s

Figure 4.28 Representative stress-strain plots for stressing rate groups stored in deionized water.

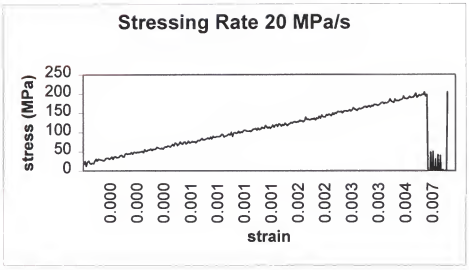

c) stressing rate of 20 MPa/s

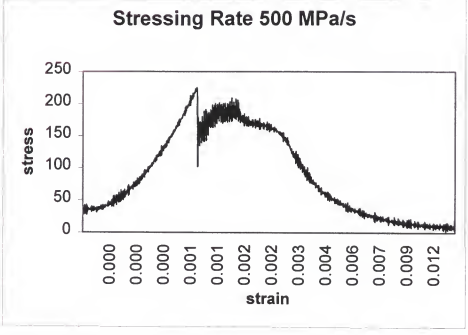

d) stressing rate of 500 MPa/s

Figure 4.28 Representative stress-strain plots for stressing rate groups stored in deionized water.

4.3 Fractal Analysis

4.3.1 Modified Slit Island Analysis

Figure 4.29 shows the fractal dimensional increment, D*, of the middle layer of the *Strombus gigas* specimen stored in aqueous environments prior to fracture obtained using the atomic force microscope. Using ANOVA, no difference was determined between any of the specimens stored in aqueous solutions. The mean fractal dimensional increment for the group stored in air had statistically significant difference from all the aqueous groups except for the mean of the group stored in pH 4 buffer. The mean D* values ranged from 0.16 for the specimens stored in air to 0.22 for the specimens stored in deionized water and specimens stored in artificial seawater.

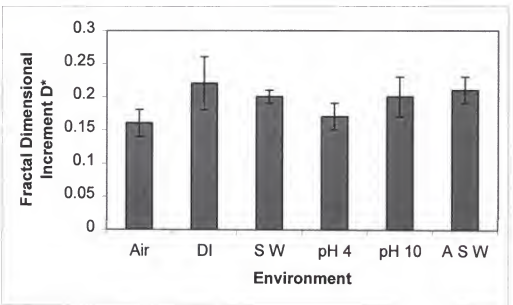

Figure 4.29 Fractal dimensional increment as a function of environment as measure by the modified slit island analysis.

Figure 4.30 shows the fractal dimension as a function of stressing rate. No statistically significant differences were found between the mean D* values of the groups as a function of stressing rate. Though the means for the specimens stored in air were greater than the group stored in water, no statistical difference was determined.

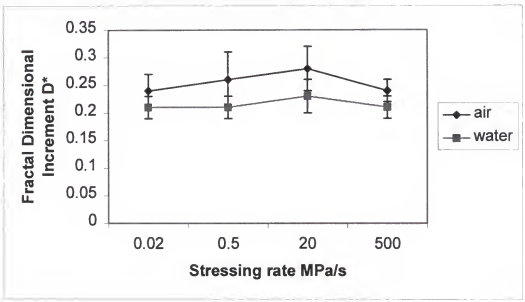

Figure 4.30 Fractal dimensional increment as a function of stressing rate as measured by the modified slit island analysis.

Figure 4.31 plots the fracture toughness obtained by the single edge notched specimen versus the square root of the fractal dimension for inner and middle layers of the *Strombus gigas*. Three conditions are represented on this plot: stored in air, stored in deionized water, and heat treated at 200°C for 24 h. The values for the middle layer for the groups stored in air and water appear to fall on the line for polycrystalline materials while all the other values are near the glass-ceramic line. This difference between the classes of materials, as approximately indicated by the solid lines, has been reported before for the baria silicate glass-ceramic system.[47] It was concluded from that study that

the reason for the change from the glass-ceramic line to the polycrystalline line on the K_{IC} versus $D^{*1/2}$ plane was the presence of an additional toughening mechanism. The two points which fall on the polycrystalline line for this study may also have a difference in mechanism due to the structure of the different layers. The middle layer has shown crack deflection while the inner later fracture surface, which has the same composition but completely different structure, demonstrates very little if any crack deflection. Though the heat treated middle layer may demonstrate a tortuous surface, the weak interfaces may prevent it from reaching the intended toughness increase from this deflection mechanism.

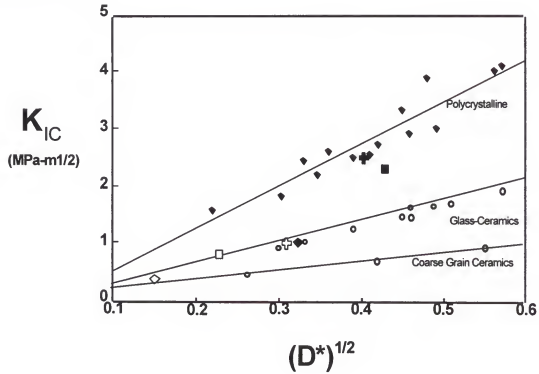

Figure 4.31 Fracture toughness versus square root of the fractal dimensional increment for both the inner and middle layers for three conditions: stored in deionized water, stored in air and heat treated. Open symbols are inner layer and filled symbols are middle layer values. Diamond – heat treated, Cross – air, and square – water.[46, 47]

4.3.2 Box Counting Technique Using the Atomic Force Microscope

Figure 4.32 shows the fractal dimensional increment obtained for the inner and middle layers using both the atomic force microscope and the modified slit island technique. The differences in mean values for the middle layer of the specimen stored in water and both layers of the specimen stored in air were statistically significant ($p \leq 0.05$) between the two techniques. Currey et al.[49] looked at a variety of bony materials using a regression step length technique over two orders of magnitude of step lengths. They suggested that the tougher materials decreased in fractal dimension as the step length decreased because of the easier separation of bony materials with a higher work of fracture at the micro level causing a crack blunting mechanism. This appears to be the case in the *Strombus gigas* for the groups stored in air and water.

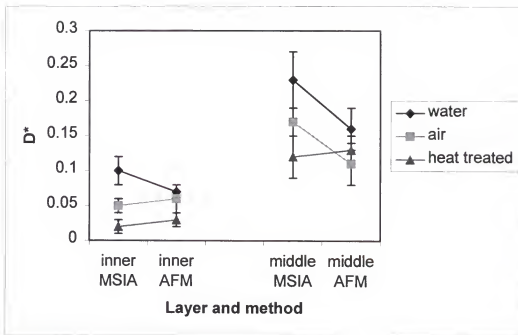

Figure 4.32 Fractal dimensional increment obtained for inner and middle layers using both a macroscopic technique (modified slit island) and a microscopic technique (atomic force microscopy)

CHAPTER 5
CONCLUSIONS

The objectives of this study were to 1) estimate the relative increase of mechanical properties from the structure and proteinaceous interface of the *Strombus gigas*, 2) determine if the aqueous solutions produced the same increase in work of fracture compared with variable pH and ion concentration, 3) identify if water activates any viscoelastic effects from the proteinaceous matrix, and 4) identify if the fractal dimension can discern if toughening mechanisms are present in the complex composite.

Based on the results of this study, the following conclusions can be made:

1. Using three conditions of the *Strombus gigas* (stored in air, stored in water, and heat treated to remove the proteinaceous interface), it was determined that the proteinaceous matrix produced a 10-fold increase in work of fracture and a four-fold increase in strength over the *Strombus gigas* without the presence of the protein.
2. The means were not statistically different between specimens stored in aqueous solutions for any mechanical property studied, while means of the strength and work of fracture all increased between the group stored in deionized water compared with the group stored in air, indicating that the primary influence of the water is to act as a plasticizer.

3. Water appears to activate the protein matrix with respect to viscoelasticity for the range of stressing rates in this study. The work of fracture increased with decreasing stressing rate when the specimens were stored in water, but decreased with decreasing stressing rate when stored in air.
4. The fractal dimension demonstrated a change of "family of material" lines on the K_{IC} versus $D^{*1/2}$ plane for the different first order structures when the protein matrix was present, indicating a change in toughening mechanisms.

In addition, I found that:

1. The models for brittle composites accurately described the stress-strain curves obtained for these specimens. The heat treated specimen group acted like a weak interface brittle/brittle composite; the group stored in air acted like a strong interface brittle/ductile composite, and the groups stored in water acted like a weak interface brittle/ductile composite.
2. When the protein was present in the structure, the fractal dimensional increment was much greater for the modified slit island analysis (MSIA) than for the box counting method of surfaces obtained from the atomic force microscope (AFM). The low toughness heat-treated group remained constant for both the MSIA and AFM methods. This finding agrees with what Currey[49] determined using multiple Richardson plots on various types of bone. He implied that the tougher antler materials peeled at the higher magnification rather easily producing low fractal dimensional increments, but not at the lower magnifications. This peeling appears to be the case with the protein of the *Strombus gigas*.

3. Visual evidence of another toughening mechanism (crack bridging) not seen previously in the *Strombus gigas* for the groups stored in an aqueous solution of ductile bridging. Previously, the major proposed mechanisms for the *Strombus gigas* have been multiple cracking and crack bridging for specimen stored in air.

The significance of these finding is that: 1) the relative contributions of the structure, protein matrix, and water to the mechanical properties of a biological composite can be determined and the mechanism of each of these can be determined using composite analysis; 2) the water appears to activate the viscoelastic component of the protein producing greater strains to failure and work of fracture; and 3) the fractal dimension can be used to discern between changes in toughening mechanisms present even in a complex composite system such as the *Strombus gigas*.

APPENDIX
CALCULATED DATA

Table 1. Data from *Strombus gigas* four-point flexural specimen stored in air.

Specimen #	Whole (MPa)	Middle (MPa)	Composite (MPa)	WOF (kJ/m^2)
102	26.01	87.68	54.47	2.68
104	10.40	239.44	110.65	5.88
105	60.09	257.14	137.18	4.05
106	29.19	137.71	76.96	4.78
107	44.51	208.28	111.83	3.16
108	58.76	187.79	109.34	12.25
109	43.41	252.43	128.83	4.62
110	12.60	134.32	68.62	1.86
111	40.30	131.97	79.19	5.38
112	36.09	141.74	81.48	7.55
113	20.75	121.93	66.83	2.95
114	121.78	213.11	144.03	4.69
117	9.29	44.15	27.61	0.88
118	74.51	130.39	92.57	2.57
121	103.79	253.15	152.54	3.54
123	30.31	230.95	115.19	4.31
124	28.14	235.29	116.05	9.73
average	44.11	176.91	98.43	4.76
std	31.57	65.19	33.97	2.86

Table 2. Data from *Strombus gigas* four-point flexural specimen stored in artificial seawater.

Specimen #	Whole (MPa)	Middle (MPa)	Composite (MPa)	WOF (kJ/m^2)
269	26.35	100.98	60.33	8.80
270	75.40	435.41	210.61	7.43
271	119.21	282.76	169.76	8.51
272	74.55	209.27	124.11	4.04
273	43.57	107.82	70.49	6.07
274	51.25	155.23	93.21	6.12
275	46.71	113.35	74.12	6.28
276	33.61	104.60	64.95	3.25
277	125.69	255.33	161.77	8.45
278	64.20	211.21	120.79	11.38
279	61.41	146.53	93.80	4.53
280	149.75	330.58	199.27	13.90
283	119.42	248.43	156.74	15.53
284	106.54	140.01	109.34	11.31
285	61.84	200.17	115.49	4.08
287	12.43	115.09	60.40	6.94
288	30.96	184.98	97.04	3.83
289	56.04	162.24	97.99	3.60
290	53.02	147.98	90.98	9.45
291	105.02	326.40	180.91	3.74
average	70.85	198.92	117.60	7.36
std	37.86	90.56	46.89	3.56

Table 3. Data from *Strombus gigas* four-point flexural specimen heat treated at 200°C for 24 h.

Specimen #	Whole (MPa)	Middle (MPa)	Composite (MPa)	WOF (kJ/m^2)
294	31.23	50.56	40.50	0.46
297	29.52	42.68	36.20	0.41
298	23.51	84.99	52.23	0.67
299	8.57	17.89	14.67	0.20
301	11.83	42.21	27.89	0.76
302	8.55	20.53	15.97	0.56
303	9.59	16.10	14.28	0.24
305	8.91	16.36	14.08	1.22
307	10.76	18.87	16.24	0.32
308	10.52	20.18	16.77	1.05
309	16.38	38.62	28.34	1.52
310	26.79	47.33	37.07	0.39
312	14.28	23.52	20.22	0.13
314	39.84	44.87	41.80	0.31
average	17.88	34.62	26.88	0.59
std	10.33	19.48	12.70	0.41

Table 4. Data from *Strombus gigas* four-point flexural specimen stored in deionized water.

Specimen #	Whole (MPa)	Middle (MPa)	Composite (MPa)	WOF (kJ/m^2)
173	38.12	209.22	109.65	11.75
174	68.50	245.52	135.93	8.27
175	115.78	377.56	204.12	18.85
176	42.57	206.35	110.28	8.77
177	29.67	178.89	94.05	13.51
178	74.23	210.38	124.41	14.63
179	124.79	230.94	152.08	11.78
181	18.47	385.53	170.53	11.95
182	101.14	304.27	171.07	13.69
183	66.85	126.58	87.89	6.12
184	67.89	196.95	116.61	7.22
185	66.02	154.63	98.94	6.22
186	127.75	374.45	207.42	17.56
187	61.00	195.23	113.19	9.14
188	33.09	108.16	66.23	10.98
189	135.92	363.52	206.39	11.06
190	38.30	285.86	139.88	7.15
191	141.73	192.33	143.71	11.20
192	100.26	200.91	130.91	10.22
193	175.66	356.27	218.43	17.19
194	26.15	385.61	173.47	12.79
195	59.71	204.22	116.25	11.56
196	88.69	237.37	140.61	7.07
average	78.36	249.16	140.52	11.25
std	42.80	86.80	41.73	3.58

Table 5. Data from *Strombus gigas* four-point flexural specimen stored in pH4 buffer solution.

Specimen #	Whole (MPa)	Middle (MPa)	Composite (MPa)	WOF (kJ/m^2)
221	134.02	351.16	167.03	11.76
222	72.56	225.36	109.28	4.73
224	33.09	198.24	87.69	5.31
225	49.26	221.87	100.68	10.78
226	25.45	266.96	107.52	6.29
228	49.35	217.43	99.27	11.34
229	30.04	172.35	78.06	5.66
230	184.86	311.50	170.37	16.08
231	61.81	317.58	134.85	15.23
232	45.06	218.05	98.08	7.88
233	231.51	321.02	187.03	19.20
234	19.82	237.09	96.07	4.95
235	24.49	149.55	68.46	7.07
236	139.39	296.36	152.12	6.08
237	57.81	278.18	121.33	12.44
238	20.50	244.48	98.69	5.46
239	74.00	273.97	125.08	15.84
240	65.29	311.13	133.94	9.19
241	37.39	225.58	98.03	5.50
242	108.97	376.45	167.10	12.53
243	77.65	298.37	133.81	12.08
244	76.66	216.84	107.87	11.20
average	73.59	260.43	120.11	9.85
std	55.34	58.26	32.22	4.28

Table 6. Data from *Strombus gigas* four-point flexural specimen stored in pH10 buffer solution.

Specimen #	Whole (MPa)	Middle (MPa)	Composite (MPa)	WOF (kJ/m^2)
245	52.24	438.59	216.17	14.29
246	78.12	144.15	105.13	6.29
247	56.28	277.52	152.20	16.21
248	129.61	246.19	169.54	6.70
249	33.29	80.11	56.99	5.19
250	58.91	215.13	127.19	20.13
251	30.69	162.57	92.56	9.15
252	40.17	243.71	131.34	8.42
253	58.87	157.40	102.54	4.20
254	112.97	233.77	157.57	5.21
256	25.38	166.31	91.88	8.14
257	118.15	203.71	147.24	3.58
258	52.08	161.00	101.16	8.00
259	58.99	283.80	155.93	5.58
261	90.26	263.83	160.60	17.00
262	29.66	100.65	64.67	6.69
264	73.56	460.88	233.59	13.19
265	178.11	223.25	180.00	6.97
266	56.34	118.90	84.68	2.09
267	48.07	205.00	118.30	12.74
268	88.39	242.78	151.11	13.00
average	70.01	220.44	133.35	9.18
std	38.40	95.12	46.07	4.90

Table 7. Data from *Strombus gigas* four-point flexural specimen stored in seawater.

Specimen #	Whole (MPa)	Middle (MPa)	Composite (MPa)	WOF (kJ/m^2)
197	25.67	273.48	154.39	8.38
199	202.62	383.67	288.67	12.81
200	53.92	258.45	160.73	8.89
201	25.25	183.23	110.30	3.91
202	70.13	204.17	142.43	9.42
203	14.91	112.16	69.63	8.33
204	128.26	208.05	172.15	12.75
205	29.84	183.37	112.68	6.72
206	57.65	259.53	163.03	8.60
207	99.79	183.80	146.91	12.24
208	83.59	283.85	186.93	6.65
210	98.58	262.47	183.90	4.79
211	92.09	284.97	191.48	5.82
212	23.00	162.71	99.10	2.68
213	207.03	422.94	308.62	7.27
214	27.94	356.31	194.87	9.40
215	41.50	224.49	138.41	7.76
216	66.94	243.42	159.76	3.34
217	181.14	368.10	271.67	9.93
218	132.52	213.88	176.96	8.63
219	134.30	193.63	168.16	11.46
220	185.36	357.01	268.51	9.23
average	90.09	255.62	175.88	8.14
std	62.0289	80.46	61.30	2.86

Table 8. Data from *Strombus gigas* stressing rate four-point flexure in water.

stressing rate 0.02	specimen #	Whole (MPa)	Middle (MPa)	WOF(kJ/m^2)
	502	73.58	263.24	7.65
	503	67.14	152.62	8.65
	504	74.71	204.52	14.66
	505	43.38	243.38	11.15
	506	109.35	251.13	9.73
	507	65.81	259.64	17.69
	508	124.59	385.82	14.93
	509	92.42	266.19	7.37
average		81.37	253.31	11.48
std		26.09	65.99	3.84
stressing rate 0.5	specimen #	Whole (MPa)	Middle (MPa)	WOF(kJ/m^2)
	521	61.67	172.82	8.77
	522	48.25	215.22	11.95
	523	100.83	354.76	17.56
	524	77.14	264.44	12.78
	526	81.53	210.71	13.51
	527	58.65	148.52	8.27
	529	72.52	234.06	10.22
	530	59.84	271.51	11.56
average		70.05	234.01	11.83
std		16.54	64.21	2.96
stressing rate 20	specimen #	Whole (MPa)	Middle (MPa)	WOF(kJ/m^2)
	531	86.43	227.27	10.98
	533	82.10	178.08	7.15
	534	103.65	301.83	14.63
	535	70.47	186.99	6.22
	537	44.56	203.68	9.14

Table 8–continued.

stressing rate 20	specimen #	Whole (MPa)	Middle (MPa)	WOF(kJ/m^2)
	538	91.76	308.19	11.25
	539	64.49	147.67	7.07
	540	79.56	208.22	10.27
average		77.88	221.96	9.59
std		18.11	57.33	2.79
stressing rate 500	specimen #	Whole (MPa)	Middle (MPa)	WOF(kJ/m^2)
	511	45.95	105.60	4.88
	512	78.34	182.82	8.55
	513	68.04	158.55	7.36
	514	48.91	116.26	5.98
	515	34.49	309.25	11.29
	516	69.80	197.66	5.85
	517	110.99	370.59	11.72
	518	80.31	225.01	8.00
average		67.10	208.22	7.95
std		24.13	91.86	2.50

Table 9. Data from *Strombus gigas* stressing rate four-point flexure in air.

stressing rate 0.02	specimen #	Whole (MPa)	Middle (MPa)	WOF(kJ/m^2)
	77	52.76	160.79	2.05
	79	60.31	70.31	2.32
	80	54.95	154.37	2.81
	83	31.10	120.77	3.13
	84	32.50	149.08	3.01
	85	79.59	109.59	2.48
	86	29.67	152.78	3.83
	87	74.50	134.50	2.39
	88	65.46	125.46	0.90
	89	24.82	66.59	0.50
	90	23.28	68.24	1.54
	91	25.50	195.19	5.39
	92	35.47	134.40	4.08
	93	23.53	85.56	0.61
	94	27.91	91.01	2.09
	95	50.83	157.18	1.92
	96	44.22	146.04	2.63
average		43.32	124.82	2.45
std		18.63	37.64	1.25
stressing rate 0.5	specimen #	Whole (MPa)	Middle (MPa)	WOF(kJ/m^2)
	51	36.27	220.92	4.03
	52	105.91	184.33	4.08
	53	117.35	272.15	4.49
	54	107.65	323.92	3.77
	56	49.71	229.64	5.89
	59	69.01	119.08	4.56
	60	77.86	209.86	4.33
	62	106.59	248.32	4.22
	63	54.03	162.68	2.68
	64	68.87	119.03	2.55

Table 9–continued.

stressing rate 0.5	specimen #	Whole (MPa)	Middle (MPa)	WOF(kJ/m^2)
	65	37.91	94.78	1.30
	66	39.83	214.37	3.09
	67	32.82	293.32	2.44
	68	50.64	289.66	4.96
	69	57.91	212.87	4.81
	70	58.31	123.34	3.76
	71	60.11	197.27	4.56
	72	24.53	33.40	2.59
average		64.18	197.16	3.78
std		28.38	76.98	1.13
stressing rate 20	specimen #	Whole (MPa)	Middle (MPa)	WOF(kJ/m^2)
	25	28.77	82.22	0.62
	26	118.46	362.42	5.02
	29	28.29	169.71	4.50
	31	28.95	256.29	4.93
	32	66.64	183.24	0.99
	33	48.47	128.01	1.18
	35	38.90	67.18	0.74
	36	33.02	227.84	4.70
	37	22.24	94.81	1.65
	38	81.95	359.18	9.19
	39	82.19	198.38	3.17
	41	74.29	204.24	3.78
	43	22.44	140.07	3.21
	44	61.23	164.45	4.32
	45	117.04	325.08	3.44
	46	111.24	121.24	5.01
	47	43.44	198.99	6.30
	48	43.68	93.25	1.01
average		58.40	187.59	3.54
std		32.63	90.74	2.27

Table 9–continued.

stressing rate 500	specimen #	Whole (MPa)	Middle (MPa)	WOF(kJ/m^2)
	1	43.90	356.69	4.79
	2	57.25	169.63	3.11
	3	18.31	104.17	2.60
	4	18.30	59.13	0.97
	7	82.62	181.41	4.51
	11	29.39	40.22	0.58
	12	76.20	248.31	7.74
	13	20.69	52.25	0.59
	14	146.66	166.66	3.31
	15	27.82	157.79	5.27
	16	89.25	259.34	5.02
	17	32.03	272.59	3.16
	18	65.81	208.58	2.76
	19	21.43	258.53	5.80
	21	54.64	329.92	3.82
	22	61.49	368.98	10.27
	23	82.62	181.41	4.51
average		54.61	200.92	4.05
std		34.24	101.70	2.48

Table 10. Fracture toughness determination using single edge notch beam.

specimen #	load	thickness (mm)	width (mm)	i1	i2	i3	crack (mm)	Y factor (N)	Kic ($MPa \cdot m^{1/2}$)	std. dev.
DRY MID										
601	42.39	3.27	5.96	789	444	75	1.58	2.56	2.57	
602	9.62	2.96	5.98	729	434	114	1.42	2.55	0.67	
603	24.44	2.02	5.81	573	387	175	0.94	2.49	2.99	
604	6.66	2.66	5.88	585	255	56	1.66	3.63	0.90	
606	46.08	2.41	5.79	691	528	259	0.91	2.16	3.39	
608	40.12	2.55	5.97	690	481	165	1.02	2.22	2.78	
609	25.97	2.18	5.93	598	404	142	0.93	2.31	2.46	
610	58.51	2.78	5.78	712	516	239	1.15	2.28	3.84	
								Mean =	2.45	0.75
DRY IN										
611	52.36	5.18	5.29	850	486	30	2.30	2.39	0.80	
615	14.29	5.79	5.99	886	536	5	2.30	2.22	0.14	
618	15.40	1.81	5.85	639	491	375	1.01	3.05	1.48	
619	15.84	1.69	5.74	672	312	37	0.96	3.10	1.76	
620	3.84	3.36	5.9	605	445	336	2.00	3.34	0.16	
								Mean =	0.87	0.37
WET IN										
621	33.66	2.45	5.97	671	598	291	0.47	1.86	0.72	
623	3.848	3.33	5.88	773	382	207	2.30	4.49	0.24	
624	26.77	3.32	5.59	760	413	237	2.20	4.10	1.59	
625	11.36	5.47	6.04	840	120	30	4.86	9.25	0.77	
626	126.82	3.39	6.05	745	634	206	0.70	1.87	1.71	
627	18.82	2.48	5.60	553	469	155	0.52	1.88	0.45	
628	47.26	3.00	5.58	660	482	184	1.12	2.15	1.29	
629	9.76	1.96	5.7	553	416	235	0.84	2.33	0.57	
630	28.24	3.10	5.97	651	471	165	1.15	2.14	0.68	
								Mean =	0.89	0.34
WET MID										
631	4.96	2.48	5.63	618	416	264	1.42	3.13	0.64	
632	18.46	4.97	5.81	808	300	27	3.23	3.93	1.09	
633	50.34	5.78	5.71	914	300	19	3.97	4.41	2.78	
634	35.47	2.10	5.79	504	402	209	0.73	2.08	2.96	
635	24.06	5.08	5.91	841	442	67	2.62	2.74	0.84	
636	34.60	3.31	5.89	640	306	127	2.16	3.94	3.72	
637	16.29	2.65	5.91	562	316	245	2.06	6.05	4.09	
638	5.25	2.32	5.87	631	471	318	1.19	2.71	0.59	

Table 10–continued.

specimen #	load	thickness (mm)	width (mm)	i1	i2	i3	crack (mm)	Y factor (N)	Kic ($MPa \cdot m^{1/2}$)	std. dev.
639	14.98	3.07	5.59	744	383	280	2.39	6.09	3.21	
640	12.82	5.74	5.56	896	667	13	1.49	1.93	0.20	
								Mean =	2.01	0.74
BURN IN										
642	4.47	2.54	6.00	625	497	205	0.77	2.00	0.24	
643	31.27	3.59	5.77	655	552	150	0.73	1.87	0.81	
644	2.30	2.21	5.06	622	451	302	1.18	2.86	0.35	
645	4.65	6.55	5.73	807	525	142	2.78	2.31	0.09	
646	10.08	2.56	5.94	539	389	214	1.18	2.46	0.83	
647	3.32	3.26	5.63	700	463	217	1.60	2.60	0.22	
								Mean =	0.42	0.21
BURN MID										
651	42.89	6.71	6.28	819	364	113	4.32	3.86	1.46	
652	69.42	5.43	5.68	691	438	105	2.34	2.34	1.78	
653	10.51	4.58	5.87	775	482	160	2.18	2.53	0.38	
655	3.97	2.32	6.06	557	358	230	1.41	3.47	0.60	
656	48.27	4.50	6.10	796	464	181	2.43	2.90	2.12	
658	4.04	4.87	5.08	777	534	131	1.83	2.16	0.12	
659	4.47	3.11	5.81	651	450	208	1.41	2.43	0.27	
								Mean =	0.96	0.40

REFERENCES

1. M Sarikaya and IA Aksay, *Biomimetics: Design and Processing of Materials*, AIP Press, New York. (1995)

2. OB Bøggild, "The Shell Structure of the Mollusks," *K. Dan. Vidensk. Selsk. Skr. Copenhagen*, 2, 232-235. (1930)

3. JD Currey, "Mechanical Properties of Mother of Pearl in Tension," *Proc. R. Soc. Lond.*, B [196] 443-463. (1977)

4. JD Currey, "Mechanical properties of mollusc shell," In *The Mechanical Properties of Biological Materials* (*Symp. Soc Exp. Biol.* 34) pp. 75-97. Cambridge University Press, Cambridge (1980).

5. JD Currey, AJ Kohn, "Fracture in the Crossed-Lamellar Structure of *Conus* Shells," *Journal of Materials Science*, 11, 1615-1623. (1976)

6. AP Jackson, JFV Vincent, RM Turner, "The Mechanical Design of Nacre," *Proc. R. Soc. Lond.*, B [234] 415-440. (1988)

7. VJ Laraia, AH Heuer, "Novel Composite Microstructure and Mechanical Behavior of Mollusk Shell," in *J. Am. Ceram. Soc.*, 72 [11] 2177-79. (1989)

8. H Kessler, L Spearing, AH Heuer, "Optimization of a Structural Composite by Mimicking the Structure of the *Strombus gigas* Conch Shell," *ASME Advances in Bioengineering*, 28, 39-48. (1994)

9. H Kessler, R Ballarini, RL Mullen, LT Kuhn, AH Heuer, "A Biomimetic Example of Brittle Toughening: (I) Steady State Multiple Cracking," in *Computational Materials Science*, 5, 157-166. (1996)

10. MD Thouless, E Olson and A Gupta, *Acta. Metall. Mater.*, 40 [6], 1287. (1992)

11. LT Kuhn-Spearing, H Kessler, SM Spearing, R Ballarini, and AH Heuer, "Fracture Mechanisms of the *Strombus gigas* Conch Shell: Implication for the design of brittle laminates," *J. Mater. Sci.*, 31, 6583-6594. (1996)

12. S Kamat, X Su, R Ballarini, and AH Heuer, "Structural Basis for the Fracture Toughness of the Shell of the Conch *Strombus gigas*," *Nature*, 405, [6790] 1036-1040. (2000)

13. R Menig, MH Meyers, MA Myers, and KS Vecchio, "Quasi-static and Dynamic Mechanical Response of *Strombus gigas* (conch) Shells," *Materials Science and Engineering*, A297, 203-211. (2001)

14. MP Harmer, HM Chan, GA Miller, "Unique Opportunities for Microstructural Engineering with Duplex and Laminar Ceramic Composites," *J. Amer. Ceram. Soc.*, 75 [7], 1715-1728. (1992)

15. IW Donald and PW McMillan, "Review, Ceramic-Matrix Composites," *J. Mater. Sci.*, 11, 949-972. (1976)

16. DC Clupper, *Tampe Case Bioactive Metal-Ceramic Laminates for Structural Application*. PhD Dissertation, University of Florida, Gainesville, Florida. (1999)

17. Z Chen and JJ Mecholsky, Jr., "Toughening by Metallic Lamina in Nickel/Alumina Composites," *J. Amer. Ceram. Soc.*, 76 [5], 1258-1264. (1993)

18. R Lakshminarayanan, DK Shetty, and RA Cutler, "Toughening of Layered Ceramic Composites with Residual Surface Compression," *J. Amer. Ceram. Soc.*, 79 [1], 79-87. (1996)

19. RM Yttergren, *Mechanical Properties of Laminated Ceramic Composites*. Thesis PhD, Royal Institute of Technology, Stockholm, Sweden. (1999)

20. AG Evans, "Perspective on the Development of High-Toughness Ceramics," *J. Am. Ceram. Soc.*, 73 [2], 187-206. (1990)

21. KK Chawla, *Ceramic Matrix Composites*, Chapman & Hall, New York. (1993)

22. LJ Schioler and JJ Stiglich Jr., "Ceramic Matrix Composites: A Literature Review," *Am. Ceram. Soc. Bull.*, 65 [2], 289-292. (1986)

23. WJ Clegg, K Kendall, and N McN Alford, TW Button and JD Birchall, "A Simple Way to Make Tough Ceramics," *Nature*, 347, 455-457. (1990)

24. KM Prewo, JJ Brennan, and GK Layden, "Fiber Reinforced Glasses and Glass-Ceramics for High Performance Applications," *Am. Ceram. Soc. Bull.*, 65 [2], 305-313. (1986)

25. DJ Mitchell, "Processing and Properties of a Silicon Nitride Multilayer Composite Toughened by Metallic Laminae," PhD Dissertation, University of Florida, Gainesville, Florida. (2000)

26. DM Robertson and DC Smith, "Compressive Strength of Mandibular Bone as a Function of Microstructure and Strain Rate," *J. Biomechanics*, 11, 455-471. (1978)

27. JC Behiri and W Bonfield, "Fracture Mechanics of Cortical Bone." In *Biomechanics: Principles and Applications* (ed. R Huiskes, D Van Campen and J Di Wijn), 247-251. Martinus Nijhoff, Den Haag. (1982)

28. WE Caler, DR Carter, "Bone Creep-Fatigue Damage Accumulation," *J. Biomechanics*, 22 [6/7], 625-635. (1989)

29. PG Fox, "The Toughness of Tooth Enamel, A Natural Fibrous Composite," *J. Mater. Sci.*, 15, 3113-3121. (1980)

30. JJ Mecholsky, TJ Mackin, DE Passoja, "Self-Similar Crack Propagation in Brittle Materials," in *Advances in Ceramics 22: Fractography of Glasses and Ceramics,* The Am. Ceram. Soc., 127-134. (1988)

31. JJ Mecholsky, DE Passoja, KS Feinberg-Ringel, "Quantitative Analysis of Brittle Fracture Surfaces Using Fractal Geometry," *J. Am. Ceram. Soc.*, 72 [1], 60-65. (1989)

32. JJ Mecholsky, "Quantitative Fractography: An Assessment." In Ceramic Transactions, 17, 413.451. *Fractography of Glasses and Ceramics I.* Edited by VD Frechette and JR Varner, American Ceramic Society, Westerville, OH. (1991)

33. JY Thompson, KJ Anusavice, B Balasubramaniam, and JJ Mecholsky, "Effect of Microcracking on the Fracture Toughness and Fracture Surface Fractal Dimension of Lithia-Based Glass-Ceramics," *J. Am. Ceram. Soc.* 78 [11], 3045-3049. (1995)

34. TJ Hill, JJ Mecholsky Jr., KJ Anusavice, "Fractal Analysis of Toughening Behavior in $3BaO \cdot 5SiO_2$ Glass-Ceramics," *J. Am. Ceram. Soc.*, 83[3], 545-52. (2000)

35. JJ Mecholsky, TJ Mackin "Fractal Analysis of Ocala Chert," *J. Mater. Sci. Lett.*, 7, 1145-1147. (1988)

36. Z Chen, JJ Mecholsky Jr., "Control of Strength and Toughness of Ceramic/Metal Laminates Using Interface Design," *J. Mater. Res.*, 8 [9], 2362-2369. (1993)

37. KC Clarke, "Computation of the Fractal Dimension of Topographic Surfaces Using the Triangular Prism Surface Area Method." *Computers and Geosciences* 122(5): 713-722 (1986).

38. KC Clarke and DM Schweizer, "Measuring the Fractal Dimension of Natural Surfaces Using a Robust Fractal Estimator." *Cartography and Geographic Information Systems*, 18, (1):37-47 (1991).

39. DR Denley, "Scanning Tunneling Microscopy of Rough Surfaces." *J. Vac. Sci. Techn.* A8(101:603-607 (1990).

40. DJ Alexander, "Quantitative Analysis of Fracture Surfaces Using Fractals." *Quantitative Methods in Fractography*. Philadelphia, ASTM. 39-51 (1990).

41. M Tanaka, "Fracture Toughness and Crack Morphology in Indentation Fracture of Brittle Materials." *J. Mater. Sci.,* 31: 749-755 (1996).

42. K Banerji and E. E. Underwood, "Fractal Profile Analysis of Heat Treated 4340 Steel." Advances Fracture Research. Oxford, UK Pergamon Press. 1371-1378 (1984).

43. EE Underwood and K. Banerji, "Fractals in Fractography." *Mater. Sci. Eng.* 80:1-14.

44. LF Richardson, "The Problem of Contiguity: An Appendix of Statistics of Deadly Quarrels." *General Systems Yearbook* 6:139-187.

45. JC Russ. *Fractal Surfaces*. Plenum Press, New York. (1994)

46. A Della Bona, TJ Hill, JJ Mecholsky, Jr. "The Effect of Contour Angle on Fractal Dimension Measurements for Brittle Materials." *J. Mater. Sci.*, 36[11]: 2645-2650. (2001)

47. TJ Hill, A Della Bona, JJ Mecholsky, Jr. "Establishing a Protocol for Optical Measurements of Fractal Dimension in Brittle Materials." *J. Mater. Sci.*, 36[11]: 2651-2657. (2001)

48. E Lespessailles, JP Roux, CL Benhamou, ME Arlot, E Eynard, R Harba, C Padonou, and PJ Meunier, "Fractal Analysis of Bone Texture on Os Calcis Radiographs Compared With Trabecular Microarchitecture Analyzed by Histomorphometry," *Calcif. Tissue Int.* 63, 121-125. (1998)

49. JD Currey, P Zioupos, and A Sedman, "Microstructure-Property Relations in Vertebrate Bony Hard Tissues: Microdamage and Toughness." In *Biomimetics: Design and Processing of Material* (ed. M Sarikaya and IA Aksay), pp. 117-144. American Institute of Physics. (1995)

50. *Standard Test Methods for Flexural Properties of Unreinforced and Reinforced Plastics and Electrical Insulating Materials*, ASTM Designation: D 790-96a, 141-149. (1997)

51 *Standard Test Method for Flexural Strength of Advanced Ceramics at Ambient Temperature*, ASTM Designation: C 1161-94. (1996)

52. RM Jones, *Mechanics of Composite Materials*, 2nd Ed. Taylor & Francis, Philadelphia. (1999)

53. SP Timoshenko, *Strength of Materials: Part II – Advanced Theory and Problems*, 3rd Ed. Krieger, Huntington, New York. (1976)

54. SP Timoshenko, *Theory of Plates and Shells*, McGraw-Hill, New York. (1940)

55. GA Thompson, "Influence of Relative Layer Height and Testing Method on the Failure Mode and Origin in a Bilayered Dental Ceramic Composite," *Dental Materials*, 16, 235-243. (2000)

56. M Srinivasan, SG Seshadri, "Application of Single Edge Notched beam and Indentation Techniques to Determine Fracture Toughness of Alpha Silicon Carbide," in Freiman SW, Fuller ER, editors, *Fracture Mechanics Methods for Ceramics, Rocks, and Concrete*, ASTM Special Technical Publication 745, American Society for Testing and Materials, Philadelphia, 46-68. (1981)

57. JD Currey, "The Mechanical Properties of Some Molluscan Hard Tissues," *J. Zool. London*, 173, 39-406 (1974)

58. Sarikaya, KE Gunnison, M Yasrebi, and IA Aksay, "Mechanical Property-Microstructural Relationships in Abalone Shell," Materials Synthesis Using Biological Processes, PC Rieke, PD Calvert and M Alper (eds) Proc MRS, Vol.174 (Materials Research Society, Pittsburgh, 109-116 (1990).

59. NV Wilmot, DJ Barber, JD Taylor, and AL Graham, "Electron Microscopy of Mulluscan Crossed-Lamellar Microstructure," *Phil. Trans. R. Soc. Lond.*, B 337, 21-35. (1992)

60. WE Caler and DR Carter, "Bone Creep-Fatigue Damage Accumulation," *J. Biomechanics,* 22 [6-7], 625-635. (1989)

BIOGRAPHICAL SKETCH

Thomas Jerald Hill was born on August 23, 1967, and is a native Floridian. Mr. Hill graduated from Boone High School in 1985, at which point he enrolled in the University of Florida. He earned his Bachelor of Science in Materials Science and Engineering in August of 1990, and his master's in materials science and engineering in May of 1998.

Mr. Hill married the former Aidines Munoz Reyes in November of 1996, and they are expecting their first child, Catherine Michelle Hill, around Thanksgiving of 2001.

I certify that I have read this study and that in my opinion it conforms to acceptable standards of scholarly presentation and is fully adequate, in scope and quality, as a dissertation for the degree of Doctor of Philosophy.

John J. Mecholsky Jr., Chairman
Professor of Materials Science and Engineering

I certify that I have read this study and that in my opinion it conforms to acceptable standards of scholarly presentation and is fully adequate, in scope and quality, as a dissertation for the degree of Doctor of Philosophy.

Kenneth J. Anusavice, Cochairman
Professor of Materials Science and Engineering

I certify that I have read this study and that in my opinion it conforms to acceptable standards of scholarly presentation and is fully adequate, in scope and quality, as a dissertation for the degree of Doctor of Philosophy.

Laurie B. Gower
Assistant Professor of Materials Science and Engineering

I certify that I have read this study and that in my opinion it conforms to acceptable standards of scholarly presentation and is fully adequate, in scope and quality, as a dissertation for the degree of Doctor of Philosophy.

Christopher D. Batich
Professor of Materials Science and Engineering

I certify that I have read this study and that in my opinion it conforms to acceptable standards of scholarly presentation and is fully adequate, in scope and quality, as a dissertation for the degree of Doctor of Philosophy.

Mark C. Yang
Professor of Statistics

This dissertation was submitted to the Graduate Faculty of the College of Engineering and to the Graduate School and was accepted as partial fulfillment of the requirements for the degree of Doctor of Philosophy.

August 2001

Pramod P. Khargonekar
Dean, College of Engineering

Winfred M. Phillips
Dean, Graduate School